energies

MDPI

Article

Validation of Actuator Line Modeling and Large Eddy Simulations of Kite-Borne Tidal Stream Turbines against ADCP Observations

Nimal Sudhan Saravana Prabahar [1,*], Sam T. Fredriksson [1,2], Göran Broström [1] and Björn Bergqvist [3]

[1] Department of Marine Sciences, University of Gothenburg, 405 30 Gothenburg, Sweden; sam.fredriksson@marine.gu.se (S.T.F.); goran.brostrom@marine.gu.se (G.B.)
[2] Swedish Meteorological and Hydrological Institute, 426 71 Gothenburg, Sweden
[3] Minesto AB, 421 30 Gothenburg, Sweden; bjorn.bergqvist@minesto.com
* Correspondence: nimal.sudhan.saravana.prabahar@gu.se

Abstract: The representation of tidal energy in future renewable energy systems is growing. Most of the current tidal turbine designs are limited by the minimum current velocity required for efficient operation. The Deep Green (DG) is a kite-borne tidal power plant designed to sustain efficient operation in tidal current velocities as low as 1.2 ms^{-1}. This could increase the geographical areas suitable for large-scale tidal power arrays. Numerical modeling of the Deep Green was carried out in a previous study using large eddy simulations and the actuator line method. This numerical model is compared with acoustic Doppler current profiler (ADCP) measurements taken in the wake of a DG operating in a tidal flow under similar conditions. To be comparable, and since the ADCP measures current velocities using averages of beam components, the numerical model data were resampled using a virtual ADCP in the domain. The sensitivity of the wake observations to ADCP parameters such as pulse length, bin length, and orientation of the beams is studied using this virtual ADCP. After resampling with this virtual ADCP, the numerical model showed good agreement with the observations. Overall, the LES/ALM model predicted the flow features well compared to the observations, although the turbulence levels were underpredicted for an undisturbed tidal flow and overestimated in the DG wake 70 m downstream. The velocity deficit in the DG wake was weaker in the observations compared to the LES. The ALM/LES modeling of kite-borne tidal stream turbines is suitable for further studies of array optimization and wake propagation, etc.

Keywords: tidal turbines; kite-borne turbines; ADCP; actuator line method; deep green; tidal power kites; virtual ADCP

Citation: Prabahar, N.S.S.; Fredriksson, S.T.; Broström, G.; Bergqvist, B. Validation of Actuator Line Modeling and Large Eddy Simulations of Kite-Borne Tidal Stream Turbines against ADCP Observations. *Energies* **2023**, *16*, 6040. https://doi.org/10.3390/en16166040

Academic Editors: Jérôme Thiebot, Eric L. Bibeau and Sylvain Guillou

Received: 12 July 2023
Revised: 10 August 2023
Accepted: 15 August 2023
Published: 17 August 2023

1. Introduction

Global tidal currents are caused by the rise and fall of sea levels due to the gravitational effects of celestial bodies [1]. It is approximated that the total energy dissipated through the tides is 3.7 TW [2]. Though only a part of the total power is feasible to harness, the tidal energy sector has the potential of becoming a considerable source of sustainable energy. One of the methods by which to harness this energy in tidal flows is tidal turbines. In terms of operation, most tidal power turbine designs share many similarities with wind power plants, whilst the latter uses air currents to generate power, the former makes use of tidal currents. A significant advantage of tidal power over wind power is the predictable nature of the tides which remain largely uninfluenced by external factors [3].

Common ways of installing tidal turbines are to mount them in barrages (sea walls) or to deploy them as tidal stream turbines (TST) [4]. The TSTs are mostly axial flow turbines and therefore require a minimum flow velocity to operate efficiently (typically > 2 ms^{-1}) [5,6], which limits the possible sites of deployment. Deep Green (DG) by Minesto AB, Gothenburg, Sweden is a kite-borne tidal turbine (see Figure 1) that can harness power from a

low-velocity tidal current. The system here studied consists of a 12 m span wing that is anchored to the sea floor with a tether, which also transmits the electrical power generated. A nacelle attached to the wing supports an axial flow turbine. The nacelle also encompasses the generator and power electronics. DG has a control system that steers it in a lemniscate (∞) pattern in a direction that is almost perpendicular to the flow (see Figure 1b). In the lemniscate trajectory, the relative flow speed through the turbine reaches up to 5–10 times the mean tidal current velocity enabling high efficiency of the turbine. The lemniscate trajectory here studied has a horizontal width of 64 m in the cross-stream direction and a vertical extent of 22 m. Eventually, these DG kites can be arranged in large arrays for efficient large-scale power generation. The power plant used in this study is the DG500 with a rated power of 500 kW deployed at the test site outside Holyhead on the west coast of Wales, where the depth is 80 m.

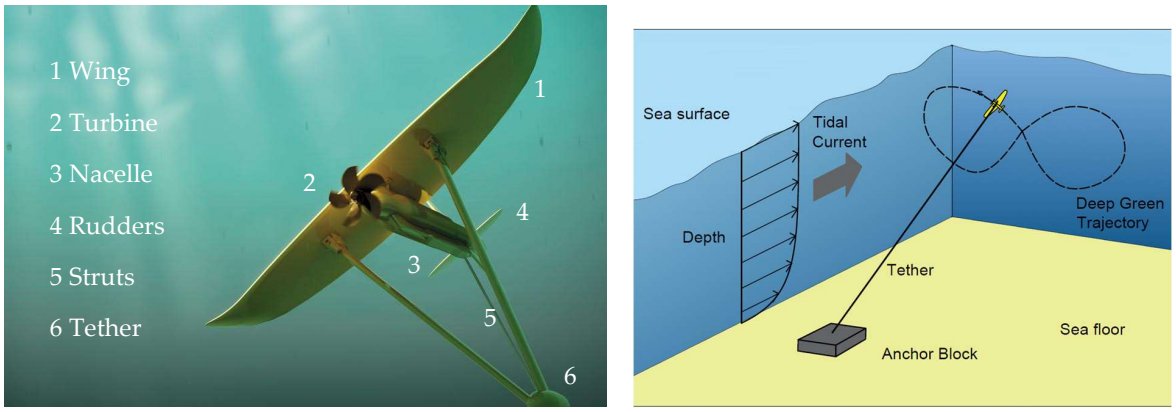

(**a**) (**b**)

Figure 1. (**a**) Deep Green kite and its parts (**b**) and the operation of Deep Green in a tidal flow (Minesto AB).

Research on tidal turbines is generally focused on two parts, the performance of the tidal turbine [7,8] and the tidal turbine wake. Studies on the wake primarily focus on wake propagation and recovery, which both have implications on array design [9]. Tidal turbine wakes have been studied using experiments and numerical methods. Model-scale experimental studies of tidal turbine wakes were conducted using flumes (e.g., [10,11]). Full-scale observations on TST wakes can be vital due to the uncertainties whilst scaling the wake from model scale tests. Since the tidal flow has been well studied via field observations [12–14], the same techniques can be used to measure TST wakes. A few full-scale observations using the acoustic Doppler profiler (ADP/ADCP) and acoustic Doppler velocimeter (ADV) were made on horizontal flow TSTs [15,16]. P. Jeffcoate et al. [17] carried out detailed observations of the velocity deficit and turbulence intensity in the wake of a horizontally mounted turbine. So far, no full-scale 'field' observations exist for kite-borne TSTs in the public domain.

Numerical prediction of TST wakes is similar to wind turbines, as both share similarities. Wind turbines benefit from a longer period of research and the numerical modeling of wind turbines has been studied extensively. The numerical models range from low-fidelity computational methods such as simplified analytical wake models [18,19] to high-fidelity methods such as computational fluid dynamics (CFD), Reynolds-averaged Navies–Stokes (RANS), and large eddy simulation (LES). Low-fidelity models such as the Jensen wake model [18] are useful in computations involving a large domain and multiple turbines, such as simulations of large arrays [20], whereas using high-fidelity computational methods facilitates the calculation of flow parameters in the near wake regime, such as the velocity deficit and the altered turbulence due to the turbines [21]. Large eddy simulations (LES) capture the turbulence produced by the blades better than RANS simulations by resolving the

largest scale of eddies. The turbine blades are usually modeled as actuator disk/line [22,23] or as fully resolved structures. Fully resolving the blade is computationally expensive; however, a wider range of turbulent structures are resolved [24].

Further, before studies on the design of power arrays consisting of multiple turbines, it is beneficial if the CFD models are validated against measurements. Such validation studies have been conducted for wind turbines [25–29]. S. Salunkhe et al. [30] carried out a validation study of unsteady RANS and improved delayed detached eddy simulation (IDDES) modeling of the tidal turbine wakes against experiments. Other validation studies of tidal turbines focused on the performance prediction of horizontal TSTs [31,32]. These validation studies lacked coverage of kite-borne TSTs so far.

Fredriksson et al. developed a numerical model for kite-borne TSTs using a further developed version of the actuator line method (ALM) combined with large eddy simulations (LES) [33,34]. The ALM, originally developed for representing wind turbines [22,23], has been validated against experimental data [35–37], but so far, not for tidal kites. Thus, the objective of this paper is to compare the ALM model for kite-borne TSTs against the ADCP (acoustic Doppler current profiler) observations made by Minesto AB in the wake of the DG500 at their installation site in Holyhead, Wales. It can act as a validation for modeling of kite-borne TSTs using ALM/LES. The ALM/LES data are computed at specific grid points, whereas the ADCP measures over an area and computes the velocity components using different beams. Hence, for a similar comparison, the numerical model data are sampled similarly to how the ADCP processes the flow recordings. The 'resampling' is conducted using a virtual ADCP (vADCP) that mimics the functioning of a physical ADCP in the numerical model.

In the following sections, the numerical model developed by Fredriksson et al. will be outlined in some detail, along with details of the ADCP observations. The resampling methodology of the vADCP is presented with a brief overview of the functioning of an ADCP. Parameters of the ADCP, such as the bin size, pulse length, and the orientation of the beam with respect to the flow, play a significant role when measuring small-scale features such as TST wakes. However, the status of these parameters during the ADCP observation of the DG wake is not known to the full extent. Thus, a sensitivity study on the impact of these ADCP parameters on the observed wake is conducted using the numerical model and the vADCP. The sensitivity study helps identify key ADCP parameters that have a significant effect on measuring TST wakes. This is followed by a discussion of the numerical model and observation data. This study acts as a proof of concept of the ALM model of DG (and kite-borne TSTs).

2. Materials and Methods

2.1. Numerical Model

2.1.1. Large Eddy Simulations (LES)

The numerical model (referred to as the 'model' in the text) developed by Fredriksson et al. [33,34] for studying tidal power kites is based on a modified version of the OpenFOAM turbinesFOAM library that is used for studying axial flow turbines [38,39]. It is based on a discretized version of spatially filtered incompressible Navier–Stokes equations modified for LES, and continuity equations, i.e.,

$$\frac{\partial \mathbf{u}}{\partial t} + (\mathbf{u}\cdot\nabla)\mathbf{u} - \nu\nabla^2\mathbf{u} = -\frac{1}{\rho}\nabla p + \mathbf{s} - \nabla\mathbf{T}, \tag{1}$$

$$\frac{\partial \mathbf{u}}{\partial x} = 0, \tag{2}$$

where $\mathbf{u} = (u, v, w)$ is the spatially filtered velocity vector in the coordinate system $\mathbf{x} = (x, y, z)$, p is the spatially filtered pressure, and ν and ρ are the kinematic viscosity and density of the fluid. LES in OpenFOAM v7 uses an implicit top hat filter that resolves the eddies larger than a set length scale, delta (Δ). Since the grid size is uniform

throughout the domain, cubeRootVol delta function is applied. cubeRootVol sets the filter length scale, Δ, as the cube root of the cell volume—in this case, the grid size of 0.625 m. In Equation (1), the term **s** is the source vector that comprises external forces such as gravity, body forces, etc. In LES, the sub-grid scale/sub-filter scales (SGS) of turbulence are modeled. Here, the SGS turbulence model is based on a single equation eddy-viscosity model represented in the equation as the tensor **T** [40,41].

2.1.2. Actuator Line Method (ALM)

Including the resolved geometry of DG in the computational domain would require a very high-resolution mesh that is computationally expensive and unsustainable [24]. Using ALM, the wing can be represented using source terms applied in the regions of the domain, where the wing/blade has its influence [22,42]. For ALM, the DG wing is split into elements in the spanwise direction (see Figure 2), and the forces in each actuator line element, i, are computed as

$$\mathbf{f}_i = \frac{1}{2}\rho U_{r,i}^2 C_i l_i (C_{L,i}\mathbf{e}_{L,i} + C_{D,i}\mathbf{e}_{D,i}). \tag{3}$$

Here, $U_{r,i}$ is the relative velocity between the wing element and the free stream, and C_i and l_i are the chord length and the span of the elements, respectively. $\mathbf{e}_{L,i}$ and $\mathbf{e}_{D,i}$ are unit vectors in the direction of lift and drag forces, respectively. Lift and drag coefficients, $C_{L,i}$ and $C_{D,i}$, are interpolated from precomputed RANS simulations. The forces are then distributed in the computational grid in a Gaussian projection sphere of radius ε (Equation (4)).

$$\mathbf{f}_{DG,i}(\mathbf{e_{r,i}}) = \frac{\mathbf{f}_i}{\varepsilon^3 \pi^{\frac{3}{2}}} \exp\left[-\left(\frac{|\mathbf{e_{r,i}}|}{\varepsilon}\right)^2\right], \tag{4}$$

where force $\mathbf{f}_{DG,i}$ is added to the source term in Equation (1). $\mathbf{e_{r,i}}$ is the unit vector from the grid point on which the source is to be applied to the center of force of the wing actuator line element. In the modified version of the turbinesFOAM [39] made by Fredriksson et al., arbitrary paths for turbine blades such as kites are implemented instead of rotational motion in wind turbines. The input trajectory data for the kite-borne TST contain the location in x, y, and z, and the orientation of the wing.

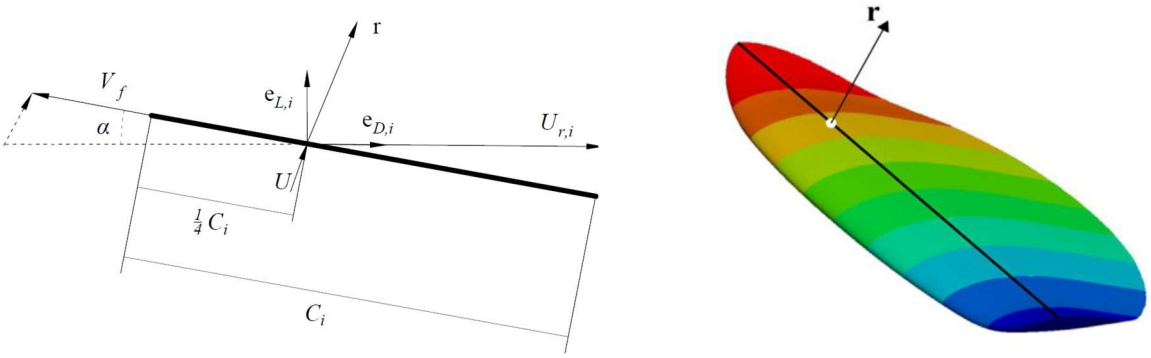

(**a**) (**b**)

Figure 2. (**a**) Line drawing of the DG element showing the direction vectors of velocity $U_{r,i}$, lift, and drag. (**b**) DG wing with the span-wise actuator line elements sketched with different colors (reworked from Fredriksson et al. [33]).

2.1.3. Computational Setup

The computational setup is based on the test site of Holyhead Deep where the average sea depth is 80 m. To accommodate the DG trajectory, the domain has a horizontal width of 240 m. The x direction is chosen as the streamwise direction with a domain length of 600 m. The side boundaries are cyclic, and the top boundary is modeled as a slip wall (rigid lid approximation for the free surface). The DG trajectory is centered at $(x, y, z) = (130, 0, 44)$ m,

and the model coordinate system is centered at the bottom of the inlet boundary (see Figure 3).

At the initial conditions, the mean tidal flow velocity of 1.52 ms^{-1} corresponds to one hour before the tidal peak. It is a fully developed turbulent tidal flow obtained using a precursor analysis. In the precursor analysis, cyclic boundaries were used in the streamwise direction with the tidal forcing represented as a simplified sinusoidal equation i.e.,

$$\mathbf{f}_T = A_T \cos(\omega t)\mathbf{e_t}. \tag{5}$$

Here A_T and $\mathbf{e_t}$ are the tidal amplitude and direction vector of the tidal current, respectively, and ω is the tidal frequency given by $\omega = 2\pi/T$. The tidal time period T was set to 12 h for this location (Holyhead). Further details of the precursor analysis can be found in Fredriksson et al. [33,34]. The velocity field captured from the precursor run is used as a time-varying inflow condition on the inlet boundary, and the outlet boundary is set as a pressure outlet. The time-varying inlet velocity acts as the tidal forcing; hence, an additional forcing term on the momentum equations is not needed. A uniform grid element size of 0.625 m is used in all three directions for both precursor and DG simulations, which results in 960, 384, and 128 cells in the x, y, and z directions, respectively (47,185,920 cells total).

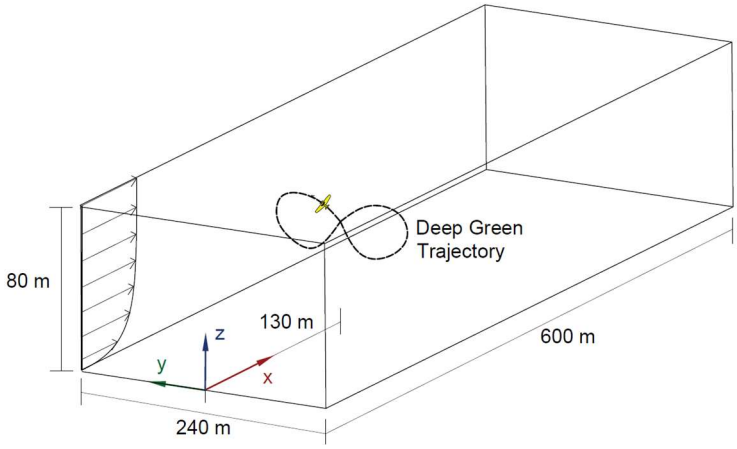

Figure 3. The computational domain used in the numerical model with the Deep Green trajectory and the coordinate system shown.

Bottom roughness is the major contributor to turbulence in tidal flows without TST. Scans of the test site showed boulders of size 1–3 m on the sea floor at a frequency of 1.6 per 100 m × 100 m, which equates to an equivalent roughness height, z_0, of 0.01 m. Instead of resolving the flow near the bottom which requires very fine grid elements, the boundary flow is modeled using wall functions, where the logarithmic law of the wall is used as an approximation for the velocity profile (Equation (6)) with a correction for the bottom roughness (included in the nutkRoughWallFunction boundary of OpenFOAM v7). The non-dimensional velocity $U^+ = U/u^*$ is based on a modified log layer, i.e.,

$$U^+ = \frac{1}{k}\log\left(\frac{Ez^+}{1 + C_S K_S^+}\right), \tag{6}$$

where K_S^+ is the non-dimensional equivalent sand grain roughness that equals $u^* K_S/\nu$ and accounts for the bottom roughness, u^* is the shear or friction velocity, and K_S is sand grain roughness that can the computed as $30 * z_0$ [43]. The roughness spacing uniformity is parametrized using C_S in OpenFOAM v7. k is the von Karmann constant with a value of 0.41, and z^+ is the non-dimensional wall distance given by $u^* z/\nu$ (z is the normal distance to the wall). ν is the kinematic viscosity of the fluid, E is a wall parameter equal to 9.81, and

u^* is the friction velocity. In the nutkRoughWallFunction, the turbulent contribution of the rough bottom is modeled as a correction to the turbulent viscosity ν_t close to the wall as

$$\nu_t = \nu \left(\frac{k\, z^+}{\log\left(\frac{Ez^+}{1+C_S K_S^+} \right)} - 1 \right). \tag{7}$$

The simulation is performed in OpenFOAM v7 using a finite volume method (pimpleFOAM solver) with a time step of 0.1 s. A second-order implicit backward scheme is used for time discretization: using current and two previous time steps. Advection and diffusion terms are discretized using a blend of 98% second-order linear and 2% first-order upwind schemes [34].

2.2. ADCP Observations

Velocity observations in the wake of the DG were conducted using a vessel-mounted ADCP by Minesto AB during the testing of the DG500 at Holyhead Deep in August 2018. The ADCP was positioned 70 m downstream of the DG trajectory. A Teledyne RD Instruments Workhorse broadband ADCP (307.2 kHz) observed data for a period of 6.5 h on 30 August 2018, with a sampling frequency of 0.455 Hz. This ADCP model has 4 beams in a Janus configuration with a beam angle (α) of 3.7 degrees and a transducer diameter (D_t) of 0.09 m. The vertical depth of 80 m was divided into 19 cells/bins of size 4 m. The ADCP parameters, pulse length, and orientation of the beams with respect to the flow were uncertain during the observations. The ADCP captured both the accelerating and decelerating tides and the DG was operational for a period of 15 min, 1 h before the tidal peak (in accelerating tide). Due to the low sampling frequency of the ADCP, certain scales of turbulence are underrepresented. For a mean flow velocity of 1.5 ms^{-1} a, using Taylors frozen eddy hypothesis, turbulent structures smaller than 3.3 m are undersampled.

2.3. Virtual ADCP

Several acoustic Doppler current profiler (ADCP) observations of currents and water discharges [44–47] have shown that it is important to be aware of the measuring conditions and parameters and the flow properties to be observed to avoid data discrepancies. ADCPs measure data over an area, and for small-scale effects such as turbine wakes where the assumption of homogenous flow does not hold, even more care has to be taken to sample the model data to match the observation techniques. Hence, to obtain a similar comparison, a virtual ADCP (vADCP) is used in the computational domain. The vADCP measures and processes the model data similar to a physical ADCP and parameters such as bin size, pulse length, orientation, and location with respect to the DG can be adjusted.

2.3.1. Physical ADCP Working Principles

A summary of the ADCP observation procedure is provided in this section. This forms the basis for modeling the virtual ADCP. ADCPs use sound waves to measure the velocity of the fluid current. ADCP consists of a transducer used to send and receive sound waves. The emitted wave from the transducer is scattered by small particles present in the water that move with the current. A portion of the scattered waves, whose frequency is shifted due to the motion of the current (i.e., Doppler shift), is reflected to the transducer. Based on the emitted and received frequencies, the relative speed, b, of the particles (here the current) parallel to the sound beam can be deduced from

$$b = \frac{f_d\, c}{2\, f_s}, \tag{8}$$

where f_s is the frequency of the sound wave, f_d is the Doppler shift in the frequency, and c is the speed of sound in that medium (~1480 ms^{-1} in water). The factor of 2 in Equation (8)

is to denote the distance travelled by the beam to and from the particle [12,13,48]. ADCPs measure velocity in its coordinate system termed the ADCP coordinate system (x_a, y_a, z_a), which is aligned with the beams and the velocity $\mathbf{u_a} = (u_a, v_a, w_a)$ (see Figure 4). The beam can only measure the velocity component parallel to the beam; hence, if the beam was sent vertically downward on the current, only the vertical component of the current velocity, w_a, could be measured (see Figure 4a). To measure the streamwise velocity component u_a, a combination of beams angled as in Figure 4b is required such that the measured velocity b_1 and b_2 is the projection of the flow velocity in the beam directions. Thus, b_1 and b_2 consist of both u_a and w_a and can be solved together to obtain the individual components assuming a homogenous flow [49]. v_a can also be deduced the same way by using two beams angled away from each other in the cross-stream direction (see Figure 4c). Hence, to deduce the 3-dimensional current profile, at least 3 beams are needed (under the assumption of homogenous flow). Since w_a is measured in both beam combinations, it can be used as a redundancy check for the current homogeneity assumption.

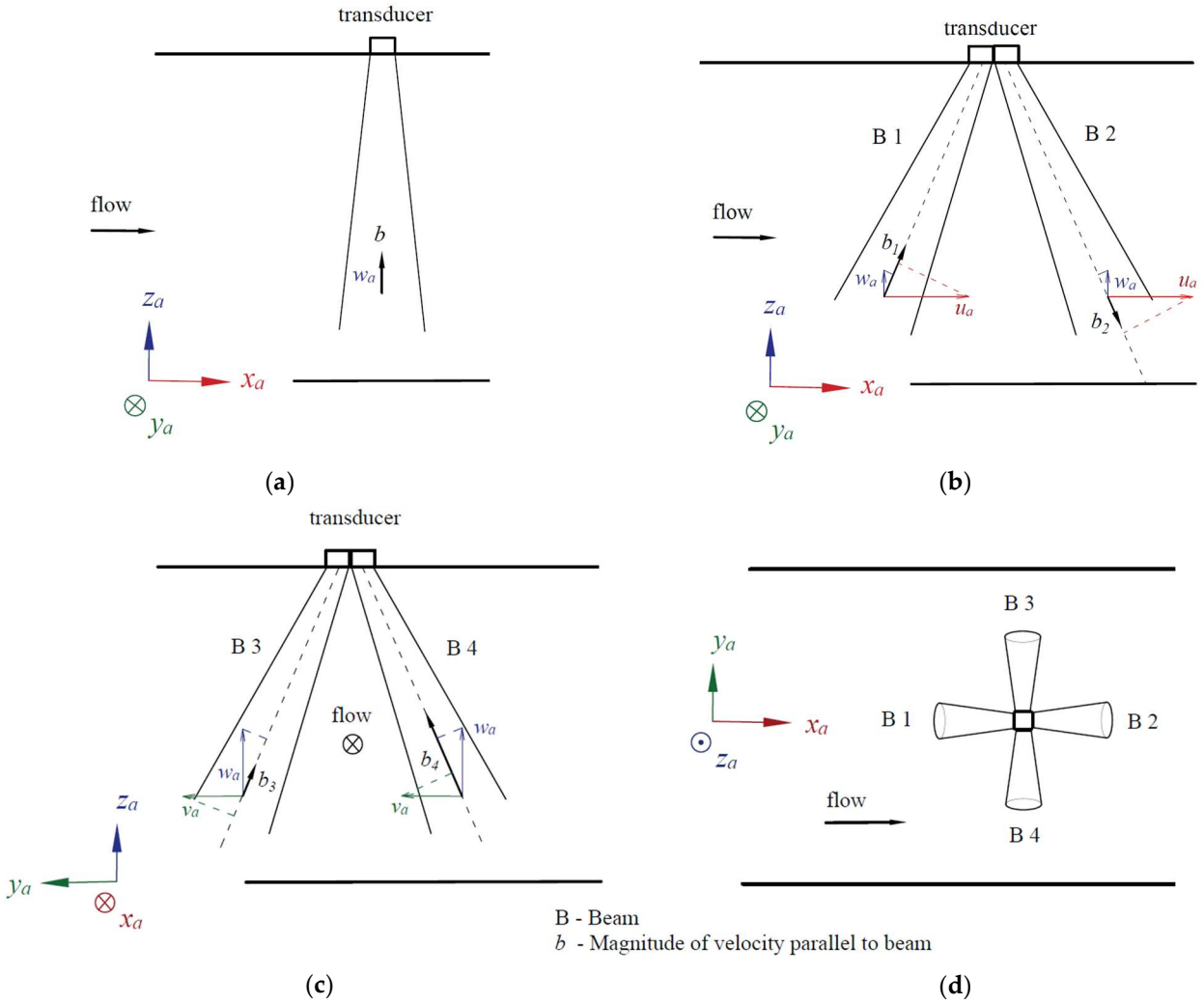

Figure 4. ADCP measured velocity and its components for (**a**) a single vertical beam; (**b**) a combination of two beams to compute stream and vertical components, u_a and w_a; (**c**) a combination of beams for measuring horizontal and vertical components, v_a and w_a; and (**d**) the orientation of beams from the top view to obtain the 3-dimensional current velocity in the ADCP coordinates.

It should be noted that the recordings in the ADCP are averaged over a depth range and the entire depth is divided into bins or cells of size l_{bin}. The transducer emits a sound pulse of length l_{pulse} and then receives signals from each bin by opening and closing time

gates corresponding to each bin [48]. Although the observations are averaged over a range, the values closer to the bin center are given higher weightage as discussed below. The transducer starts receiving when sufficient time has passed to let the head of the pulse reach a particular bin's center and scatter back to the transducer. At the same instant, the signal received by the transducer will also contain the scatters from other parts of the pulse, which have not reached the bin center yet. Since the transducer will be receiving until the pulse tail leaves the bin center, the transducer continuously receives scatters along the pulse; hence, the (averaged) range where the velocity is measured equals l_{pulse} on either side of the bin center. The portion of signals from the bin center will, however, be higher than from the bin boundaries.

2.3.2. Modeling the Virtual ADCP

The objective is to sample the model data similar to the ADCP observations, using a virtual ADCP (vADCP) in the computational domain. A similar virtual ADCP has been used for assessing the accuracy of ADCPs by Mercier et al. [50]. In this study, a vADCP in the DG wake will be used to sample the model data and compare it with the ADCP observations. Moreover, the sensitivity of the observations to ADCP parameters such as bin size, pulse length, and orientation of the beams will be studied using the vADCP. A description of the resampling method followed in this study is presented in this section.

The location and orientation of the vADCP are set relative to the model coordinate system. $\mathbf{u}(u, v, w)$ is sampled from the model at the same sampling frequency as the ADCP observations (0.455 Hz). Since the beam directions are known, the first step is to filter the grid points that will be captured by the virtual ADCP beams. The beam is centered at the location J_t relative to the model origin. With a beam angle (α) of 3.7 degrees and a transducer diameter (D_t) of 0.09 m, the beams can be represented geometrically as a cone with the apex at J_0 and a diameter of 0.09 m at the transducer (see Figure 5a). Using vector algebra, J_0 can be estimated from J_t and the beam direction unit vector ($\mathbf{e}_b$) as

$$J_0 = J_t + \mathbf{e}_b \frac{-D_t}{2\sin\left(\frac{\alpha}{2}\right)}. \tag{9}$$

The grid points that lie inside the sampling space of a beam are filtered as follows. For a grid point (m) to lie inside a beam cone, the angle between the vector from the grid point to the apex of the cone ($\mathbf{e}_m$) and the axis of the cone ($\mathbf{e}_b$) must be less than half of the beam angle (α). The filter function γ is 1 when a point is inside and 0 when it is out, and it is defined as

$$\gamma = \begin{cases} 1 & if \quad cos^{-1}\left(\frac{\mathbf{e}_m \cdot \mathbf{e}_b}{|\mathbf{e}_m|\,|\mathbf{e}_b|}\right) \leq \frac{\alpha}{2} \\ 0 & if \quad cos^{-1}\left(\frac{\mathbf{e}_m \cdot \mathbf{e}_b}{|\mathbf{e}_m|\,|\mathbf{e}_b|}\right) > \frac{\alpha}{2} \end{cases}. \tag{10}$$

To calculate the velocity component parallel to the beam at the filtered grid points, the velocity $\mathbf{u}$ at that grid point is projected onto the beam direction, and its magnitude b_n is estimated as

$$b_n = \left(\frac{\mathbf{u} \cdot \mathbf{e}_{b,n}}{\left|\mathbf{e}_{b,n}\right|^2}\right), \tag{11}$$

where b_n is the component of velocity parallel to $\mathbf{e}_{b,n}$ for each beam. The subscript n denotes the beam number (beams B1, B2, B3, and B4).

As discussed in Section 2.3.1, the ADCP data are depth gated vertically. To model depth gating in the vADCP, weight functions are used as in Equation (12). The weight function is simplified to be a linear distribution, with the bin center having the highest weight. The weight function depends on the l_{pulse} as it determines the depth range that is measured for each bin. If $l_{pulse} = l_{bin}$, the weight function is triangular with the apex at the bin center and the base extending between adjacent bin centers. There is a significant overlap between the bins, and this leads to a vertically smoothed velocity profile. If

$l_{pulse} < l_{bin}$, the weight function becomes sharper, with less smoothing over the vertical range. $l_{pulse} > l_{bin}$ causes the observations and weights to be distributed across several bins, resulting in smoother profiles [48].

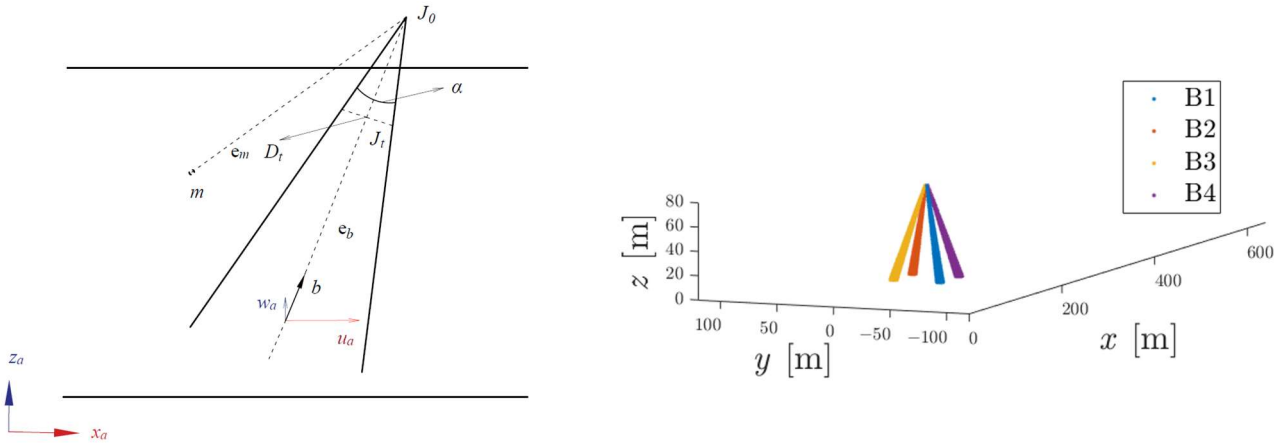

(**a**) (**b**)

Figure 5. (**a**) Beam geometry showing a grid point m outside the beam and the unit vectors $\mathbf{e}_b$ and $\mathbf{e}_m$, where J_t is the center of the beam transducer. (**b**) Filtered grid points inside the beam sampling space, filtered using Equation (10) for the four beams in the model coordinate system. B1, B2, B3, and B4 represent the four Janus-configured beams used for estimating the 3-dimensional current profile.

Since the beams measure over a wide area, there will be multiple b_n measurements at a single z coordinate. Thus, before using the weight function, all the velocity measurements at a given z location in the grid are first averaged in the x and y direction, resulting in one b_n per z coordinate. Then, the weights are distributed such that the sum of the weights is equal to the number of values averaged (N), i.e.,

$$\varphi = \begin{cases} \frac{z - z_{bin}}{l_{pulse}} + 1 & if \quad z_{bin} - l_{pulse} \leq z \leq z_{bin} \\ -\frac{z - z_{bin}}{l_{pulse}} + 1 & if \quad z_{bin} + l_{pulse} \geq z > z_{bin} \\ 0 & otherwise \end{cases}, \tag{12}$$

where z_{bin} is the z ordinate of the particular bin center, l_{pulse} is the beam length, and φ is the weight function at each z ordinate. The averaged range at each bin center extends above and below the center by l_{pulse}. To maintain even weight distribution between either side of the bin center, the weights are normalized such that the sum of the weights on either side is $N/2$ (see Equation (13)). This is required as an additional process as due to the finite nature of the grid, there might be lesser z values (grid points) on one side of the bin center than the other. We thus use the normalized weight functions:

$$\Phi = \begin{cases} \frac{\varphi * N}{2 * \sum \varphi\{z \leq z_{bin}\}} & if \quad z \leq z_{bin} \\ \frac{\varphi * N}{2 * \sum \varphi\{z > z_{bin}\}} & if \quad z > z_{bin} \end{cases}. \tag{13}$$

From the normalized weight functions, Φ, the depth-gated velocity magnitude at each bin center is estimated as

$$\langle b_n \rangle = \frac{b_n \, \Phi}{N}. \tag{14}$$

In a physical ADCP, the velocity estimate at each beam will be solved together to estimate the velocity components $\mathbf{u}_a$. Similarly, in the vADCP, the velocity components are calculated as

$$u_a \sin(90 + \beta) + w_a \cos(90 + \beta) = < b_1 >, \tag{15a}$$

$$-u_a\sin(90+\beta)+w_a\cos(90+\beta)=<b_2>, \tag{15b}$$

$$v_a\sin(90+\beta)+w_a\cos(90+\beta)=<b_4>, \tag{15c}$$

$$-v_a\sin(90+\beta)+w_a\cos(90+\beta)=<b_3>, \tag{15d}$$

where β is the elevation angle of the beam with respect to the water surface. b_1, b_2, b_3, and b_4 are the magnitude of velocities in the direction of beams 1, 2, 3, and 4. Solving the system of Equations in (15a)–(15d) will yield the velocity components u_a, v_a, and w_a, assuming that the current is homogeneous between the beams. The velocities are then rotated in the z axis by the set mount angle to obtain the velocity components in the model coordinate system. Using the z rotation matrix the velocities in stream, cross-stream and vertical directions can be obtained as

$$\mathbf{u_r}=\begin{bmatrix}u_r\\v_r\\w_r\end{bmatrix}=\begin{bmatrix}cos\psi & -sin\psi & 0\\ sin\psi & cos\psi & 0\\ 0 & 0 & 1\end{bmatrix}\begin{bmatrix}u_a\\v_a\\w_a\end{bmatrix}, \tag{16}$$

where $\mathbf{u_r}$ is the velocity in model coordinates that has been sampled using a vADCP and ψ is the ADCP mount angle (orientation with respect to the stream, see Figure 6). Since w_a could be calculated using only two pairs of Equations (15a,b) or (15c,d), it can be used to check homogeneity between the pairs of beams using an error parameter [51]:

$$\xi=|w_{a,12}-w_{a,34}|=\left|\frac{b_1+b_2-b_3-b_4}{2\cos(90^\circ+\beta)}\right|. \tag{17}$$

Here, $w_{a,12}$ and $w_{a,34}$ are the vertical velocity component calculated using Equations (15a,b) and (15c,d), respectively. Transforming ξ from ADCP to model coordinates is not required as a rotation in z does not affect the vertical components.

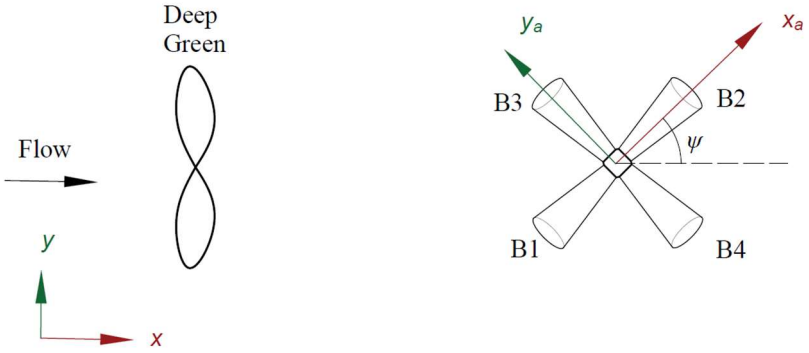

Figure 6. Position and orientation of the vADCP with respect to the tidal flow and the DG. (x, y, z) is the model coordinate system and (x_a, y_a, z_a) is the ADCP coordinate system. The orientation of the beam with the flow is defined using the mount angle, ψ.

2.3.3. Sensitivity Study of the Virtual ADCP

Since there were unknowns during the field observations, it will be beneficial to study the sensitivity of the measurements to these parameters. For the sensitivity study of the vADCP, two ψ are used: zero and 45 degrees. ψ of 45 degrees is most common in vessel-based ADCPs, and zero might be used in fixed moorings. Two common bin sizes for the Teledyne ADCPs are 4 m and 8 m; hence, these are used. The pulse length is, by default, the same as the bin size. However, it could be adjusted while setting up the ADCP. Here a l_{pulse} of 4 m, 8 m, and 16 m is used. All the parameters of the vADCP in the sensitivity study are given in Table 1.

Table 1. vADCP parameters for the sensitivity study.

Parameter	Value
Transducer width, l_t [m] *	0.09
Beam width, α [deg] *	3.7
Elevation β[deg]—with respect to the water surface *	−70
Direction vector of the beams in the local coordinates *	[−0.2418, −0.2418, −0.9397] [0.2418, 0.2418, −0.9397] [−0.2418, 0.2418, −0.9397] [0.2418, −0.2418, −0.9397]
Pulse length l_{pulse} [m]	4, 8, 16
Bin size l_{bin} [m]	4, 8
Orientation with respect to the flow, ψ [deg]	0, 45

* Parameters were kept constant during the sensitivity study.

2.4. Turbulence Intensity

Turbulence intensity is a measure of the fluctuations of flow velocity proportional to the mean flow velocity and is a critical parameter often used in studying tidal turbines [52]. Turbulence Intensity in x direction, TI_x, can be estimated as

$$TI_x = \frac{\sqrt{\overline{u'^2}}}{\sqrt{\overline{u^2 + v^2 + w^2}}}, \tag{18}$$

where u' is the fluctuation of the x-velocity, u, given by $u' = u - \overline{u}$; and the overbar denotes time-averaging. For the vADCP, $\mathbf{u_r}$ is used in Equation (18); and for the observations, the observed velocities are applied. Field measurements of instantaneous velocities using ADCP are prone to outliers and instrumentation noise [51,53,54]. Outliers in the observations are removed by omitting velocity measurements outside of 3 standard deviations from the mean flow velocity at each depth cell [55]. Instrument noise can be removed by a white noise approximation [53–55], but this has been neglected here due to the already existing uncertainties in the measurements. Further, the standard deviation of noise for this ADCP is low (~0.005 m/s) since it was a broadband ADCP.

3. Results

3.1. Numerical Model

In this section, the results from the LES/ALM numerical model without the vADCP are presented. This helps in an understanding of the structure of the Deep Green wake. In Figure 7, results from the LES model with an embedded DG are presented. The grey isosurfaces in the figures represent a magnitude of vorticity equal to 0.25. The DG is visualized by the isosurface (blue) of the ALM force field magnitude and its Gaussian projection. It can be seen that the bottom roughness is one major contributor to the turbulence (vorticity) in the flow. The forces from the DG reduce the stream velocity and generate strong vortices that are of similar, if not of larger, magnitude than the bottom turbulence. The wing tip vortices generated by the DG are structured with a periodic pattern in the immediate wake. As the vortices propagate downstream, the structure becomes more chaotic, and further downstream, the magnitude of vorticity reduces. A power plant placed in a region with strong vorticity experiences proportionally higher fluctuations of forces on its construction than a power plant in undisturbed flow. It can impact the power generation and the life of the power plants and hence can be a critical aspect in designing power plant arrays [52].

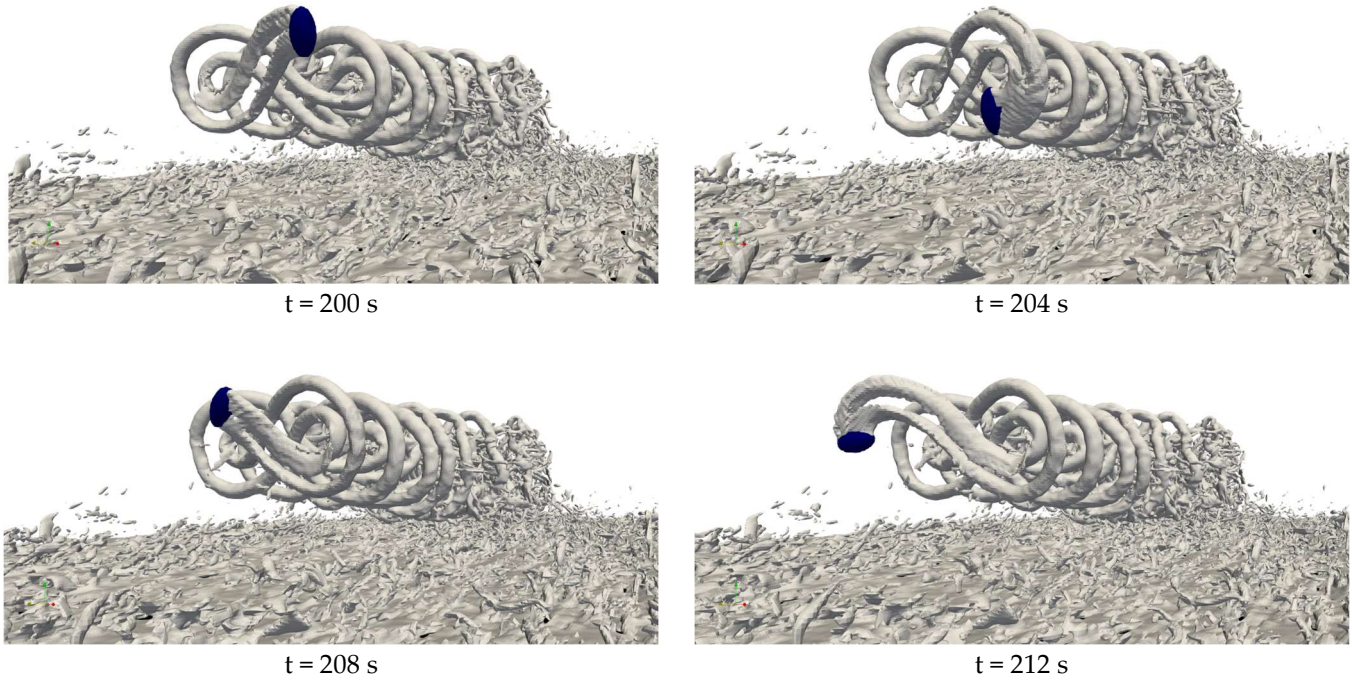

Figure 7. Numerical model results with the DG showing the magnitude of the vorticity (equal to 0.25) as a grey isosurface and DG as a blue isosurface.

To further study the impact of the DG on the flow, the instantaneous velocity is averaged over a period of time. The time-averaged x velocity ($\overline{u}$) is plotted on the yz plane at $x = 135$ m (see Figure 8) with and without the DG. Since the DG is centered at $x = 130$ m, this would be the immediate wake of the DG. The vertical gradient of $\overline{u}$ observed in Figure 8a is due to the rough bottom boundary. The presence of DG (Figure 8b) reduces $\overline{u}$, and we can see the lemniscate pattern of the DG trajectory in the wake where the velocity is less than the undisturbed flow velocity. The wake, and how it develops downstream will have a large impact on the extractable energy downstream of the first DG.

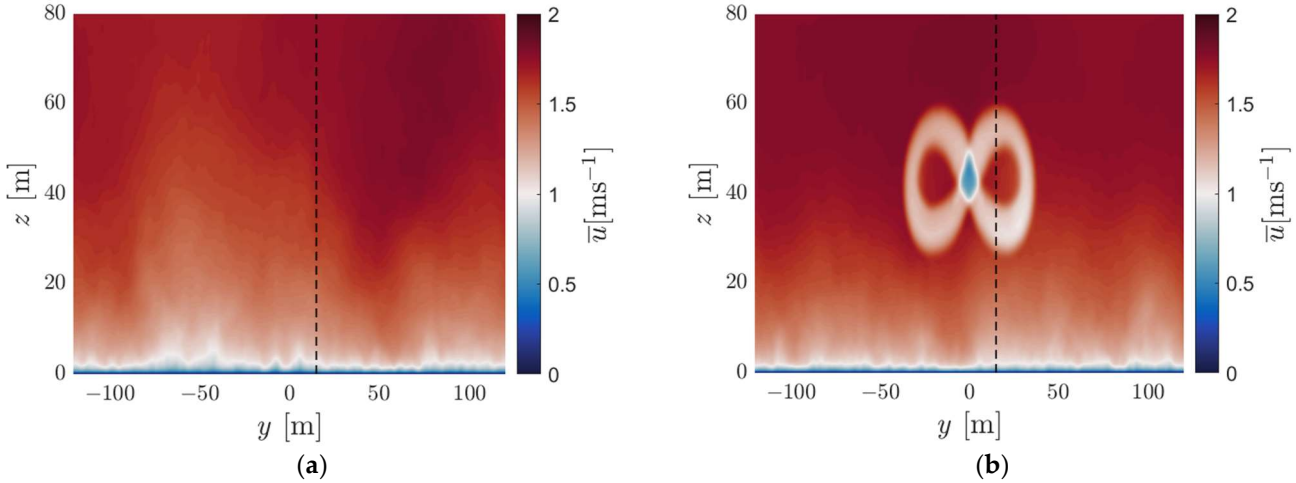

Figure 8. $\overline{u}$ from the model plotted in the yz plane at $x = 135$ m, 5 m behind the location of DG (**a**) without the DG and (**b**) with DG. The black dashed lines indicate the position $y = 15$ m, where the DG trajectory is the widest in z.

In Figure 9a, the contour of $\overline{u}$ is plotted in the xy plane at the center of the DG trajectory ($z = 44$ m). It can be seen that the strength of the wake reduces as the wake propagates

downstream. Moreover, the wake is oriented towards the trajectory center in the xy plane as it propagates. This is due to the y component of tether force acting towards the trajectory center, resulting in a flow component towards the trajectory center. In contrast, axis-symmetric turbine wakes expand away from the center as there is no inward force acting on the fluid [25]. In the xz plane, we see the wake directed towards the bottom boundary (see Figure 9b). This is due to the fact that the force (in the tether) required to maintain the DG in its trajectory can be decomposed into a vertical (z) and horizontal component (x), based on the angle between the tether and the bottom. The vertical component of the force acts downward and is responsible for the downward advection of the DG wake. Similar wake behavior has also been reported in airborne tethered kite wakes [56]. Wake expansion can be seen in the xz plane as the wake propagates downwards due to the tether force not acting inwards toward the trajectory center.

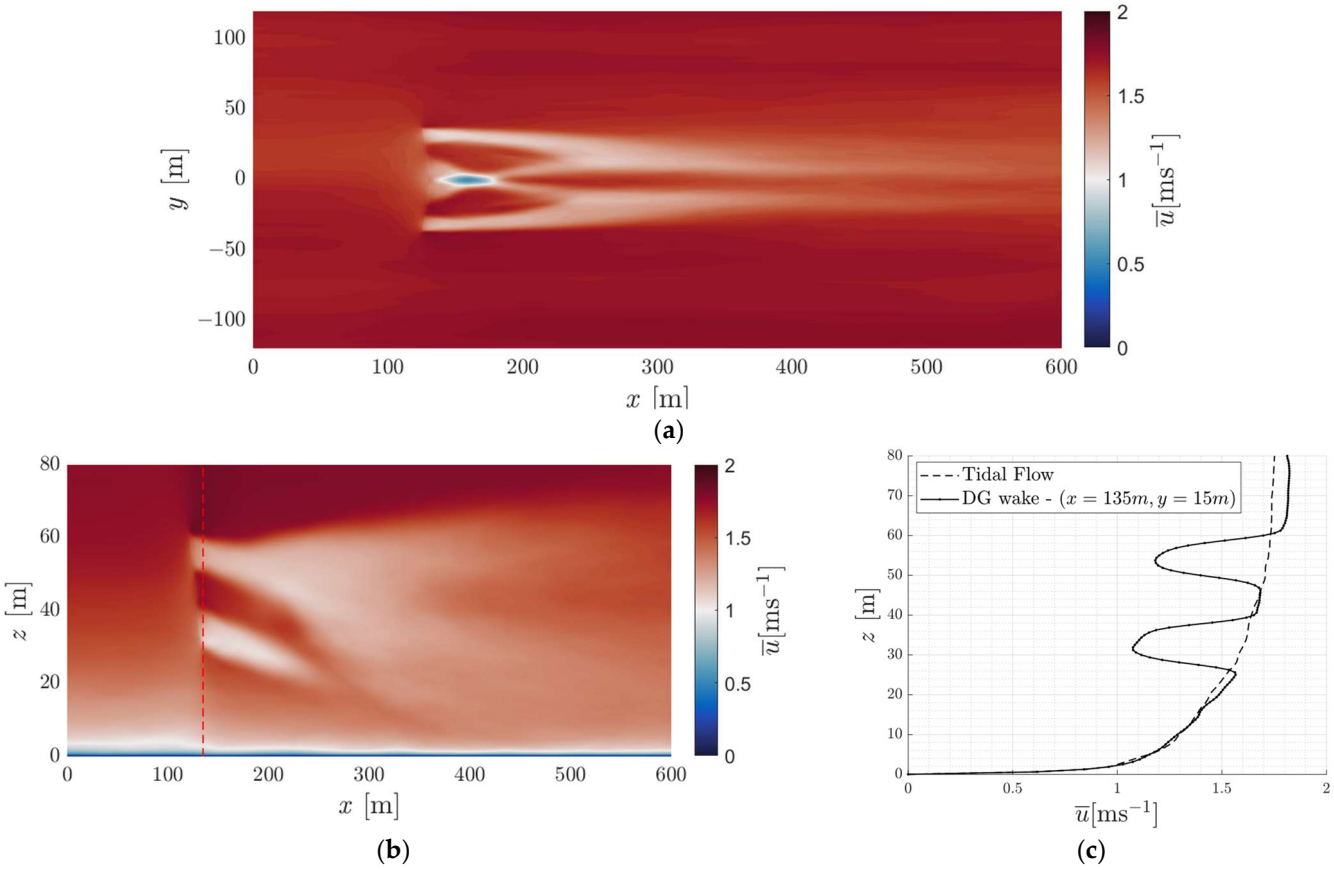

Figure 9. $\overline{u}$ from the model with the DG (**a**) in the xy plane at $z = 44$ m (center of the lemniscate) and (**b**) in the xz plane at $y = 15$ m (black dashed line in Figure 8b). (**c**) The velocity profile of $\overline{u}$ at $(x, y) = (135,\ 15)$ m (red dashed line in Figure 9b) for the undisturbed tidal flow and the flow with the DG.

The velocity profile of $\overline{u}$ 5 m downstream of the DG at $(x, y) = (135, 15)$ m (shown as a red dashed line in Figure 9b) is plotted in Figure 9c. The reduction in $\overline{u}$ in the regions where the DG operates is significant compared to the undisturbed tidal flow. Since the DG acts as a drag force slowing down the fluid, some fluid will move around the DG trajectory; the fluid thus accelerates as is seen by the higher velocities around the velocity deficit cores.

3.2. ADCP Observations

The contour plot of the stream velocity component from the ADCP observations 70 m downstream of the DG TST is presented in Figure 10. This is the entire dataset collected during the observation. The tidal period is approximately 12 h, the peak is at 11:00, and the

tide direction is negative (reversed compared to the central peak) at the start and end of the observations. DG is operational 1 h before the tidal peak (the white square in Figure 10). The operation of DG reduces the flow velocity over the trajectory, which is seen in the region encircled in Figure 10. A reduction greater than 50% is observed to be caused by the DG locally, even though the DG was operational for only 15 min.

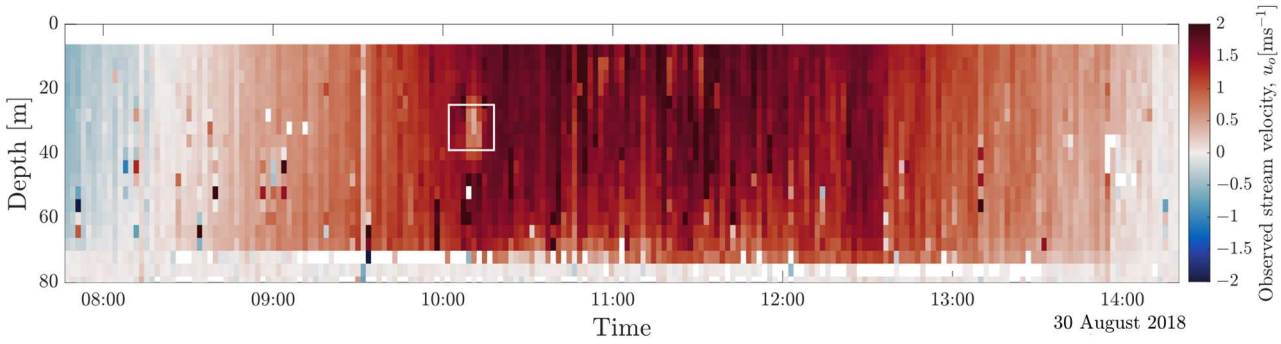

Figure 10. Observed stream velocity (u_o) contours for the full observation. The velocity reduction caused due to the DG operation is highlighted using a white square in the figure.

3.3. Sensitivity Study of the vADCP

The sensitivity of the vADCP in measuring the tidal flow, and the DG wake is studied using the time-averaged velocity and the turbulence intensity in the stream direction. In Figure 11a, the sensitivity of the stream velocity to the vADCP parameters is presented for an undisturbed tidal flow. It can be seen that the mount angle, ψ, has a negligible impact on the measured velocity profile. After time-averaging, the tidal flow is mostly homogeneous in the horizontal layer; therefore, changing the beam orientation should not affect the vertical profile. The bin size has an impact on the resolution of the profile, which becomes significant close to the bottom. However, in physical ADCP observations, values closer to the bottom are contaminated with interference, rendering them unusable. Pulse length also had a minor impact on the profiles. Higher pulse lengths lead to a smoothened profile. However, since the time-averaged tidal velocity profile is quite smooth away from the bottom, this had negligible impact on the profile.

The turbulence intensity, TI_x, profiles for the undisturbed tidal flow were affected by the vADCP parameters to a greater extent than the velocity profiles. Higher pulse lengths smoothen the measured velocity over multiple bins. Therefore, turbulence intensity, which is a measure of fluctuations, is reduced with increasing pulse lengths (see Figure 11b) in all orientations and bin sizes. By default, the pulse length equals the bin size. While using a larger bin size of 8 m, it could be better to reduce the pulse length to 4 m from the default value if turbulence intensity is of interest. As seen in Figure 11b, ψ has a considerable impact on the TI_x; there are higher values measured with ψ = 0 deg than 45 deg. With the increasing bin size, the resolution of details in the TI_x profile is reduced.

For the vADCP in the DG wake, the effect of these parameters was significant. The ψ affects the velocity profile of the measured wake significantly (see Figure 12a). With ψ = 0 deg, the beams measure the stream velocity close to the trajectory center of the DG. Hence, a single and stronger velocity deficit is seen in the velocity profile. At ψ = 45 deg, stream velocity is measured by all four beams, away from the trajectory center. The DG wake approaches an annular form away from the trajectory center as seen in Figure 8b. Therefore, velocity deficits appear at two different depths and are weaker compared to ψ = 0 deg. Substantial differences between the measured velocity profiles are seen with the varying pulse lengths as higher pulse lengths smoothen the velocity profiles.

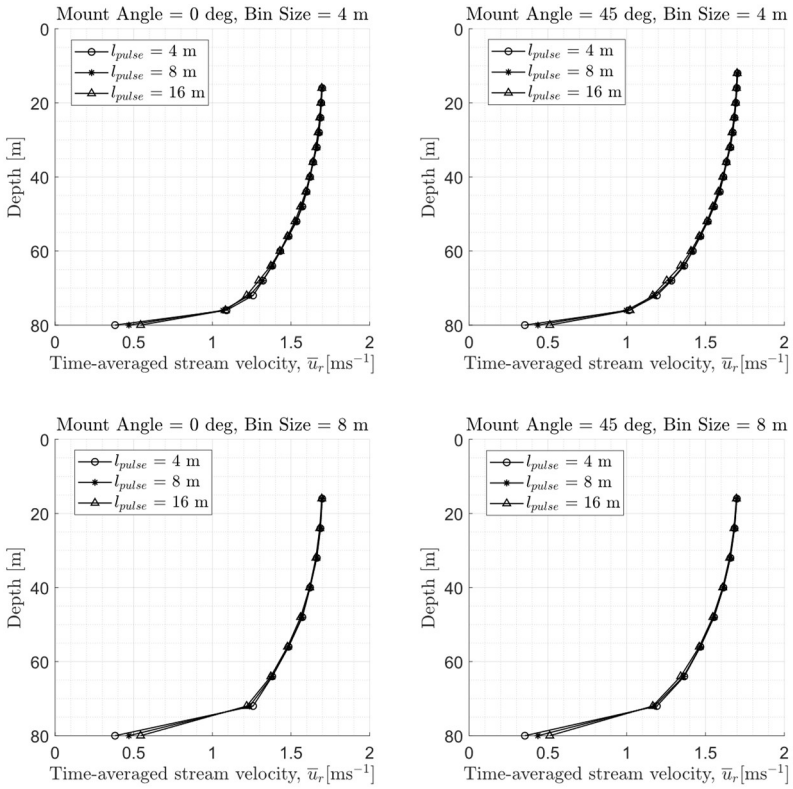

(**a**)

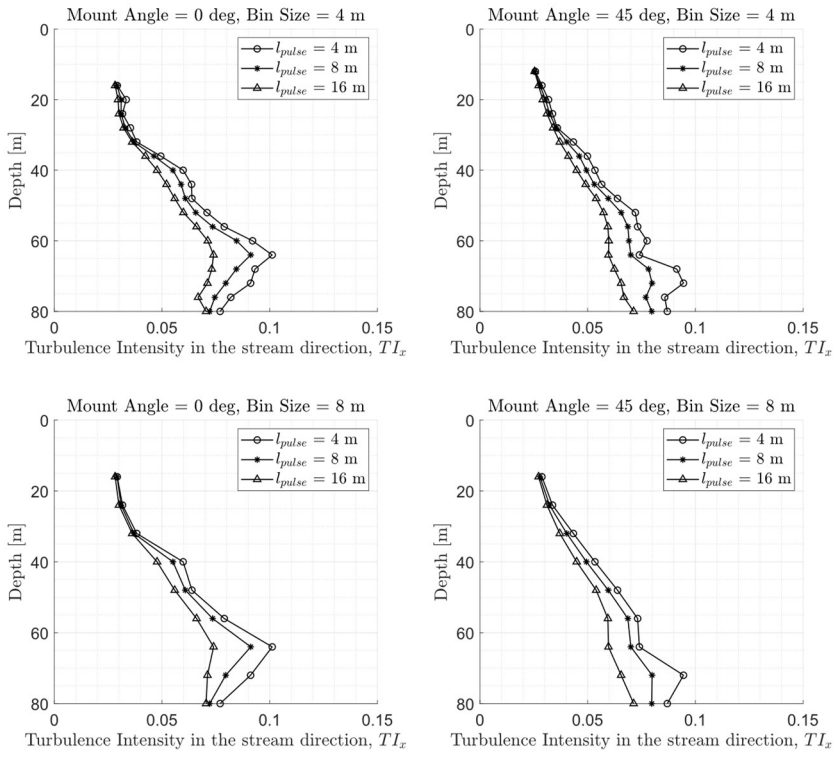

(**b**)

Figure 11. Sensitivity study of the (**a**) time-averaged stream velocity, $\overline{u}_r$ and the (**b**) stream component of the turbulence intensity, TI_x, in the undisturbed tidal flow using the vADCP.

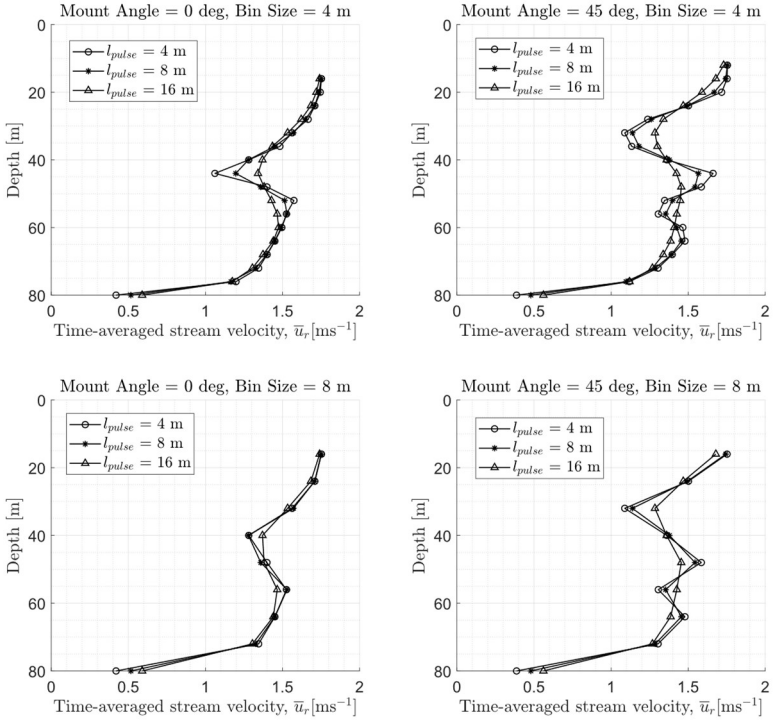

(**a**)

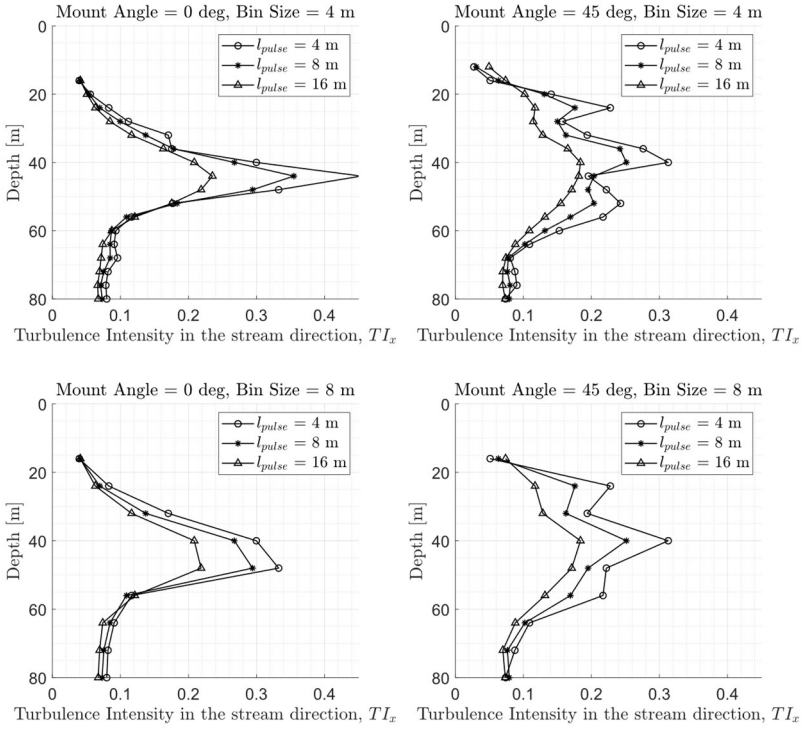

(**b**)

Figure 12. Sensitivity study of the (**a**) time-averaged stream velocity, $\overline{u}_r$, and the (**b**) stream component of the turbulence intensity, TI_x, in the DG wake using the vADCP at 70 m downstream of the DG.

In the case where ψ = 45 deg and pulse length = 16 m, the two deficits were smoothened to form a single deficit (see Figure 12a). When the bin size is increased, the measured velocity profile is of reduced resolution and not accurate for the DG wake; hence for measurements in turbine wakes, lower bin sizes could be preferred.

The measured turbulence intensity in the DG wake and its sensitivity to the vADCP parameters is shown in Figure 12b. High values of TI_x are seen in the regions where the DG operates. Similar to the velocity profiles, the mount angle has a significant impact on the measured TI_x. A single strong peak of TI_x is seen for ψ = 0 deg, and a widely distributed TI_x is seen for ψ = 45 deg. Increasing pulse lengths reduce the measured TI_x and smoothen it vertically. The cases where ψ = 0 deg and ψ = 45 deg are somewhat similar in structure for a pulse length of 16 m (see Figure 12b).

3.4. Comparision of Model Results with Observations

In this section, the ADCP observations will be compared against LES model data that have been sampled using the vADCP. The vADCP bin size, l_{bin}, is set as 4 m as this is known from the observations. For this comparison, the other vADCP parameters, pulse length and mount angle, are unknown from the observations and are assumed to be constant. Pulse length is, by default, same as the bin size; hence, it is set as 4 m. The mount angle, ψ, is assumed as 45 degrees as this is the most common way to mount vessel-mounted ADCPs to minimize hull interference.

The undisturbed tidal flow without the DG is compared between observations and the model vADCP data using the time-averaged velocity and turbulence intensity in the stream direction. Using ξ, the current homogeneity is checked for both the model and the observations. Then, the flow in the DG wake is analyzed using both instantaneous and time-averaged velocities. Turbulence intensity is also computed in the DG wake to study the effect of the DG on turbulence. Finally, the effect of the DG on the tidal flow is studied by normalizing the wake with the undisturbed tidal flow as a function of depth.

3.4.1. Undisturbed Tidal Flow

Time-averaged stream velocity is plotted in Figure 13a from both the observations and the model vADCP for the undisturbed tidal flow, i.e., without the DG. As the tidal forcing is varying, the undisturbed time-averaged velocity during the tidal phase that the DG operates is unavailable in the observations for specific flow conditions. Hence, the data are interpolated for 200 s before the DG started to operate and 200 s after DG halted its operation. Running the model with a lower mean flow velocity was not feasible in the moment since the trajectory data for the DG were available only for 1.52 ms^{-1} of mean flow; moreover, using the same trajectory and orientation in a lower mean flow can result in force imbalances. The model velocity has the same shear structure as the observed velocity, although the mean flow velocity is somewhat higher in the model. Further, in Figure 13a, the velocity profile in the model is smoother compared to the ADCP data, which show a non-monotonic increase in speed as a function of depth, even after the time averaging. The grey-shaded plots in Figure 13a correspond to 1 standard deviation (σ) from the time-averaged velocity at each depth cell.

Time-averaged error velocity ($\overline{\xi}$) is shown in Figure 13b for both the model vADCP and the observations. In both cases, $\overline{\xi}$ increases towards the bottom boundary, which could be attributed to both the increase in turbulence and the distance between opposite beams. The maximum $\overline{\xi}$ is around 0.1 ms^{-1}, which is ~7% of the mean flow. The observations have a large variance in ξ, which could be an indication of strong flow disturbances or turbulent structures with scales shorter than the distance between opposite beams. The instantaneous error velocity, ξ, in the observations reaches values greater than 0.5 ms^{-1}, indicating that the current homogeneity assumption is less valid in these observations. In the model vADCP, the maximum ξ is about half that of the observations. Higher flow fluctuations, instrument noise, and uncertainties could be the cause of the high ξ in the observations.

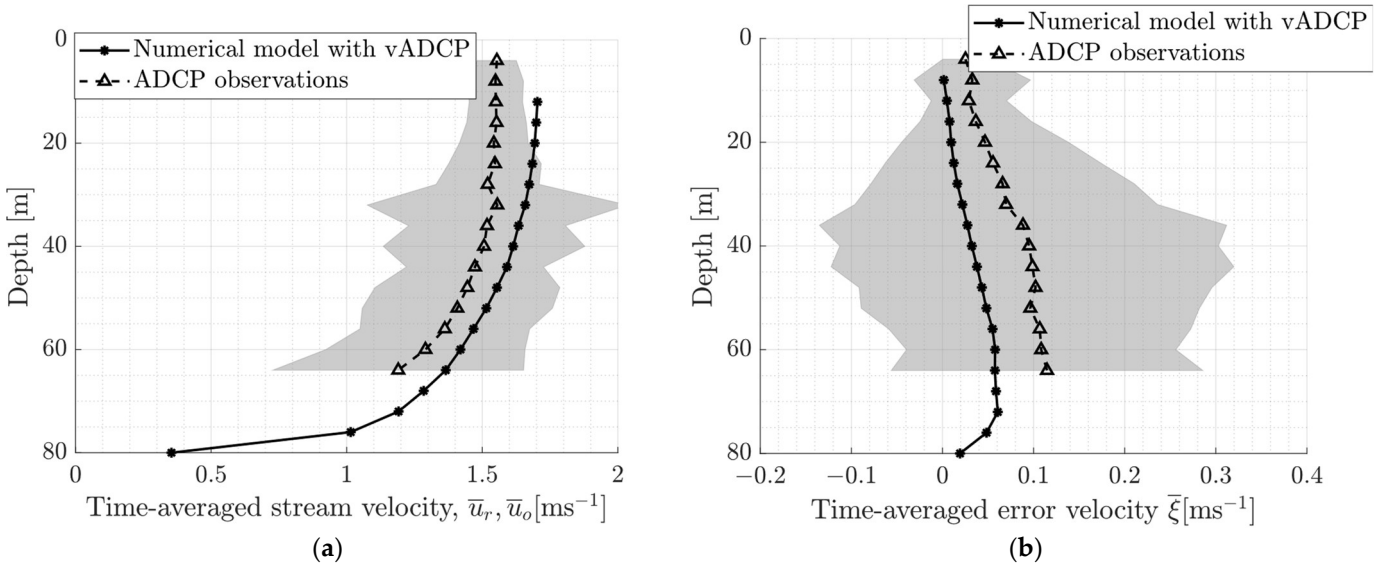

Figure 13. (**a**) Time-averaged stream velocity from the ADCP observations and the model vADCP in an undisturbed tidal flow; the grey-shaded region corresponds to the standard deviation $-\sigma$ and $+\sigma$ of observed velocity. (**b**) Time-averaged error velocity, $\overline{\xi}$, for the model vADCP and the observations in an undisturbed tidal flow; the grey-shaded region corresponds to the standard deviation $-\sigma$ and $+\sigma$ of the observed $\overline{\xi}$. $\overline{\xi}$ can be a measure of current homogeneity; the lower the $\overline{\xi}$ value, the more homogenous current in the horizontal direction.

An increase in the turbulence intensity (TI_x) is seen towards the bottom boundary in the model vADCP and the observations. The bottom roughness is the major contributor to the increased turbulence close to the bottom (see Figure 14). Higher values of TI_x indicate that the LES model underpredicted the bottom roughness. Further, contributions from the DG anchor block which was present during the whole observations is not included in the model. Turbulence near the surface is dominated by wave action and the modeling of the free surface as a slip boundary in the simulations could have contributed to the discrepancies in this region. However, these values are comparable to previous simulations in the same region [57]. The turbulence in the model is, overall, underpredicted compared to the observations for an undisturbed tidal flow.

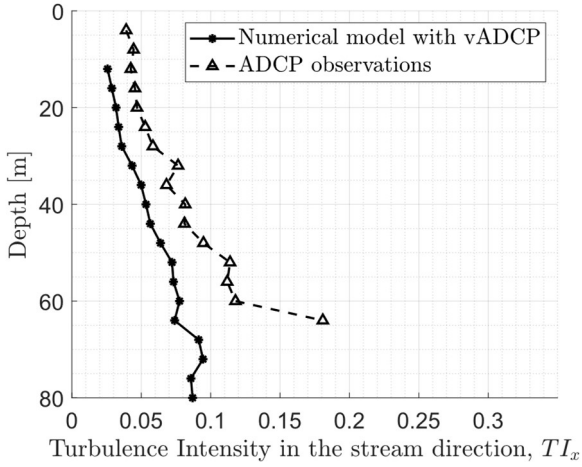

Figure 14. Turbulence intensity in the stream direction for the observations and the model vADCP in an undisturbed tidal flow: velocity observations outside three standard deviations of the mean flow velocity are omitted from the turbulence intensity calculations in the observations.

3.4.2. Flow in the Deep Green Wake

In Figure 15, the streamwise velocity measured by the physical ADCP and the model vADCP are presented. It can be seen that the propagated wake from the DG retains its periodic nature at 70 m downstream. Structured vortices are visible in the DG wake as regions of low velocity (blue) when the DG passes through the plane followed by a region of high velocity (red). As the DG operates some fluid will be deflected at a higher velocity. The alternative regions of low and high velocities could also be identified in the observations providing evidence that the DG could deflect the flow around it. There are two deficits at depth levels 50 m and 30 m that are advected in a periodic pattern. The two depth levels of deficit indicate that the ADCP is measuring the stream velocity in the wider parts of the lemniscate trajectory away from the trajectory center. The depth difference between the two deficit levels is greater in the model than in the observations, suggesting a weaker wake in the observations that has recovered earlier upstream. The time elapsed between the periodic deficits is of similar magnitude to the time period of the DG in the lemniscate trajectory (~20 s).

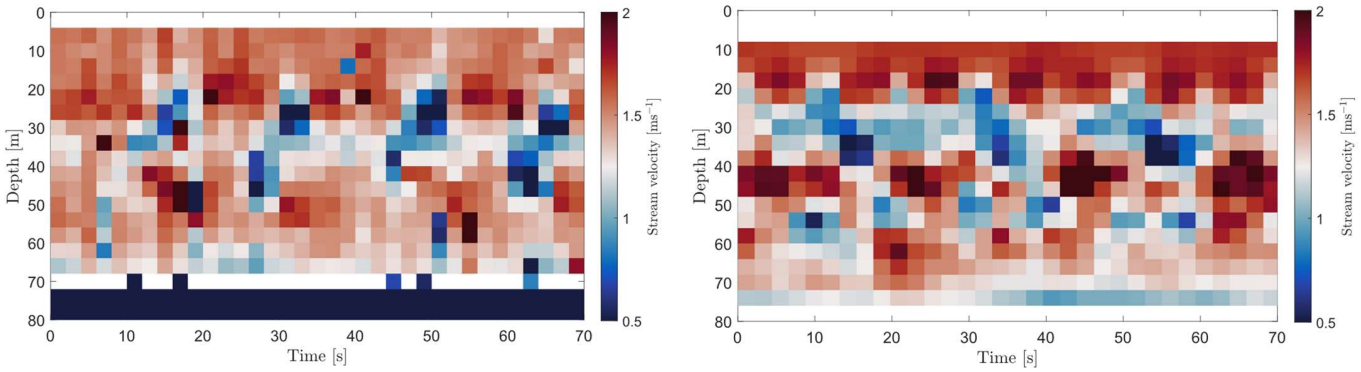

Figure 15. Instantaneous velocity showing the cyclic pattern of the DG wake in (**a**) the observations and (**b**) the model vADCP 70 m downstream of the DG. Each value in the horizontal axis corresponds to an Eulerian measurement at an interval of 2.2 s (0.455 Hz), and the vertical axis is the depth.

The instantaneous error velocities ξ when the DG is operational were significant and are as large as the tidal current velocity (~1.4 ms^{-1}) in the observations. The extreme values of ξ in the observations are not uniform, and are more localized in space, indicating that it could be an effect of noise. In the model vADCP, however, lower ξ values are seen compared to the observations, but it is twice as large as the model without the DG. These high values of ξ imply that the DG wake is highly inhomogeneous in the horizontal direction.

The time-averaged stream velocity for the model vADCP and observations in the DG wake are given in Figure 16a at a distance of 70 m downstream of the DG. The model profile has two defined regions of low velocity in the wake. In the observations, a single velocity deficit is seen, which could be due to the lower mean flow velocity and higher turbulence in the observations. The force exerted by DG can be approximated as proportional to the square of the velocity. In the x momentum equation (see Equation (1)), neglecting viscous effects and pressure losses, the velocity deficit can be approximated to be proportional to the square root of the DG forces or proportional to the current velocity [58]. Hence, the lower tidal flow during the observation compared to the model can cause a weaker velocity deficit and reduced downwash of the wake. The two deficit cores could also have been mixed upstream of the observational location in the observations due to the higher turbulence levels, as higher turbulence levels aid faster wake recovery [59]. Further, it could also be due to the orientation of the beams; a mount angle of 0 deg, instead of the assumed 45 deg, measures a single velocity deficit (see Figure 12a).

There is a large standard deviation (σ, grey-shaded plots in Figure 16a) in the ADCP observations, suggesting strong disturbances in the DG wake. The σ can be treated as a

measure of flow randomness or turbulence levels in the observations, and comparing it with the undisturbed σ in Figure 13a, there is an increase in variance in the regions affected by the DG. Such disturbances are expected since the DG wing generates strong vortices that contribute to flow turbulence. It could also be seen that the standard deviation (σ) at the DG trajectory center (see Figure 16a) is of the same order as the σ in the undisturbed flow close to the bottom in Figure 13a.

In Figure 16b, the time-averaged error velocities are plotted with the DG operational as a function of the depth. The error velocity at the depth where the DG operates is significant compared to the $\overline{\xi}$ without the DG. $\overline{\xi}$ has a maximum value of 0.35 ms^{-1} for the observations indicating that the current is not homogenous when the DG is operational. In the velocity deficit cores, the $\overline{\xi}$ is also higher because of the periodic flow fluctuations caused by the DG passing through the plane.

Comparing the turbulence intensity in stream direction, TI_x, when the DG is operational shows increased turbulence in the regions where the DG operates (see Figure 17), which is seen both in the model vADCP and the observations. Increase in TI_x caused by the DG is 2–3 times larger than the TI_x increase due to the rough bottom boundary (see Figures 14 and 17). Regions of higher TI_x correspond with the locations of increased vorticity in the DG wake. TI_x due to DG is higher in the model than in the observations. It indicates that the wake is weaker at 70 m downstream of DG in the observations compared to the model. This can be due to the lower mean flow velocity in the observations and increased wake recovery due to higher upstream turbulence in the observations.

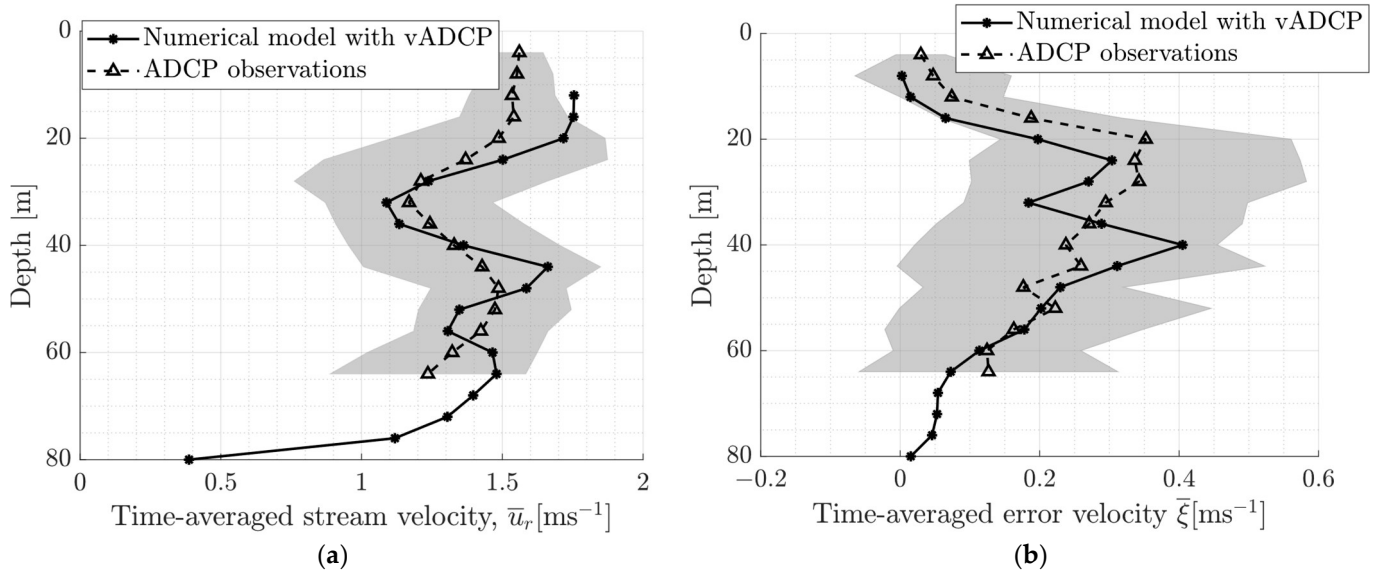

Figure 16. (**a**) Time-averaged stream velocity from the ADCP observations and the model vADCP in the DG wake (70 m downstream); the grey-shaded region corresponds to the standard deviation $-\sigma$ and $+\sigma$ of observed velocity. (**b**) Time-averaged error velocity, $\overline{\xi}$, for the model and the observations in the DG wake; the grey-shaded region corresponds to the standard deviation $-\sigma$ and $+\sigma$ of the observed $\overline{\xi}$. $\overline{\xi}$ can be a measure of current homogeneity; the lower the $\overline{\xi}$ value, the more homogenous the current in the horizontal layer.

Plotting the time-averaged stream velocity of the DG wake against the undisturbed flow will aid a deeper understanding of the DG wake and its impact on the flow. Figure 18a shows the time-averaged stream velocity of the model vADCP with the DG and undisturbed tidal flow. In the region below the velocity deficit, there is an increase in the velocity. A similar pattern can be seen in the observed data as well (see Figure 18b), suggesting that flow velocity increases around the DG trajectory.

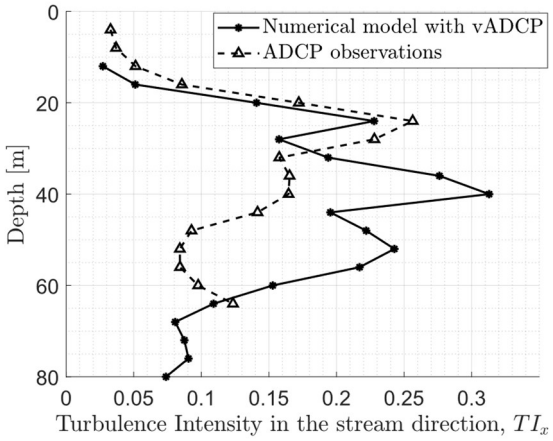

Figure 17. Turbulence intensity in the stream direction for the observations and the model vADCP in the DG wake (70 m downstream). Velocities outside three standard deviations of the mean flow velocity are omitted from the turbulence intensity calculations for the observations.

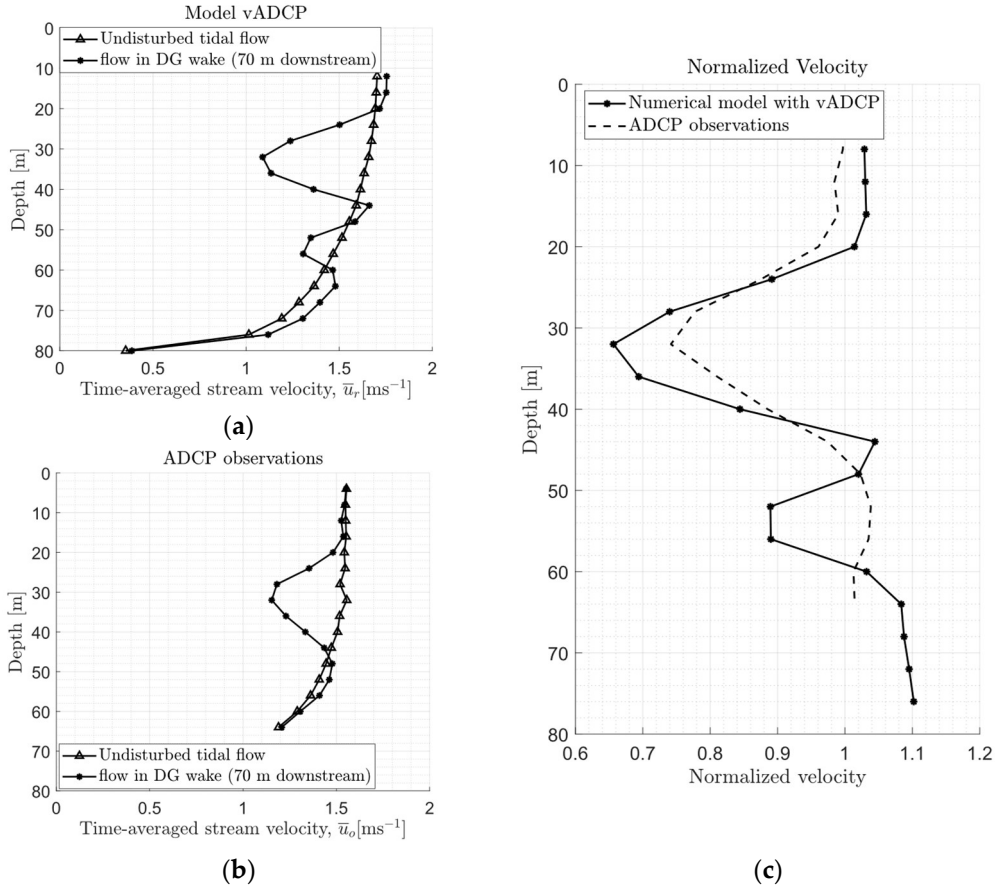

Figure 18. Time-averaged stream velocity (**a**) from the model vADCP and (**b**) the ADCP observations for undisturbed tidal flow and flow with the DG. (**c**) Model and observational velocity with DG, normalized with the undisturbed velocity ($\overline{u}^{DG}(z)/\overline{u}^{UG}(z)$). The velocities are measured at 70 m downstream of the Deep Green.

Normalizing the flow with DG using the undisturbed flow at each z coordinate ($\overline{u}^{DG}(z)/\overline{u}^{UG}(z)$) isolates the deviation of the velocity due to the effects of DG. The superscript DG indicates the velocity with the DG in the flow, and UD represents the undisturbed flow. The normalized velocities of the model and observations are shown in Figure 18c. The velocity deficit caused by the DG is at the same vertical location for both the model

vADCP and the observations. However, the strength of the velocity deficit is lower in the observations, and it could be due to the lower mean flow velocity and lower forces on the DG. Normalized velocity in the region above the DG trajectory (z = 60 to 80 m) shows good agreement between the model and observations, indicating that modeling the free surface as a slip wall in the model was reasonable for these simulations. In the regions below the trajectory, there is an increase in velocity from the undisturbed flow velocity which is seen both in the model and the observations. This indicates that the effects of the DG on the tidal flow are well predicted by the model; however, the LES/ALM model overestimates the wake at 70 m downstream.

Similarly, the turbulence intensity with the DG and the undisturbed flow for the observation and the model are plotted in Figure 19a,b. The TI_x is increased by a factor of 2–3 due to the presence of the DG. In both the model and the observations, TI_x is reduced close to the bottom in the DG wake (see Figure 19a,b). As there is an increase in the flow speed outside the trajectory of the DG (see Figure 18a,b) compared to the undisturbed flow, the TI_x values will be lower as the fluctuations are normalized with the flow speed. Normalizing the DG TI_x with the undisturbed TI_x, the change in turbulence due to DG can be isolated (see Figure 19c). The normalized TI_x is higher in the model than in the observations; this could be due to the higher undisturbed TI_x in the observations; hence, normalizing with it reduces the normalized TI_x. This indicates that the increased turbulence due to the DG on the tidal flow is overestimated by the LES/ALM model 70 m downstream of the DG.

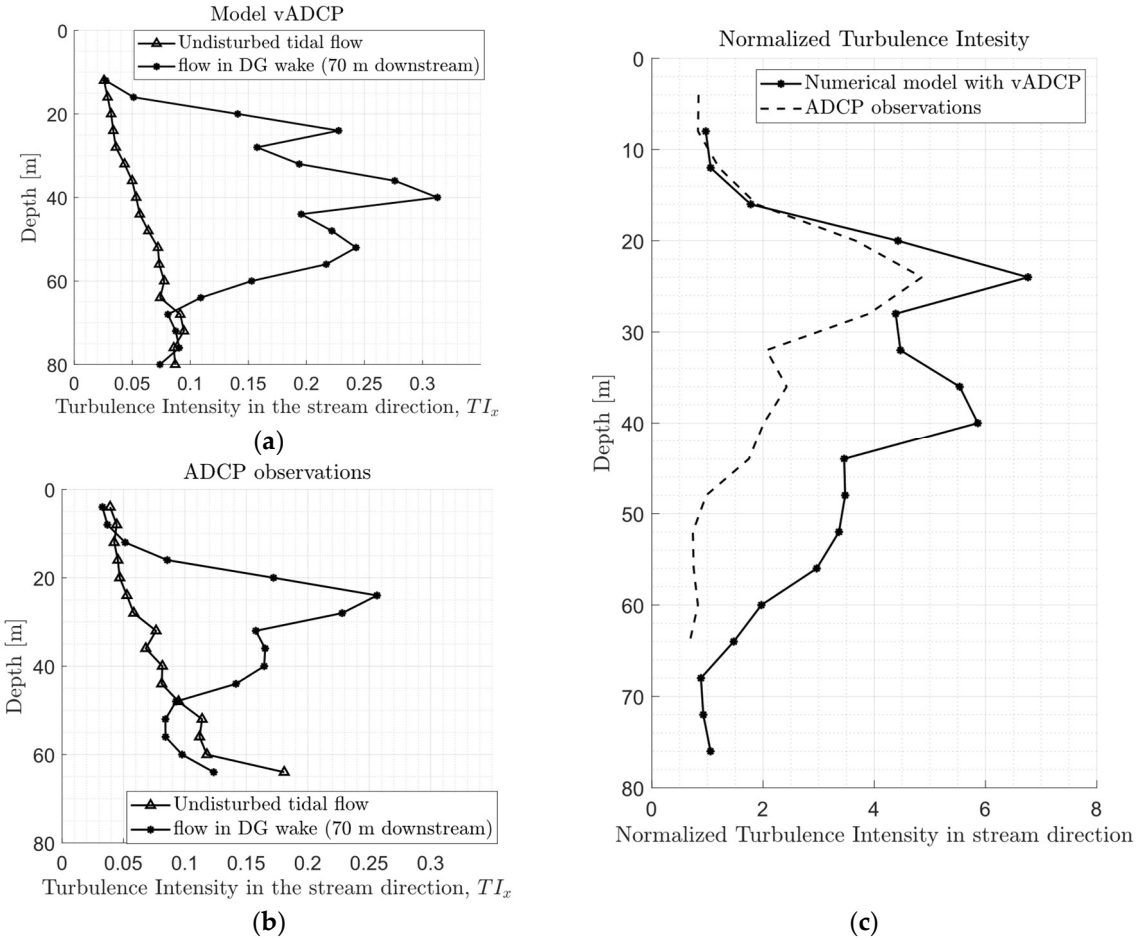

Figure 19. Turbulence intensity in the stream direction, TI_x, (**a**) from the model vADCP and (**b**) the ADCP observations for undisturbed tidal flow and flow with the DG. (**c**) Model and observational TI_x with DG, normalized with the undisturbed TI_x (${TI_x}^{DG}(z)/{TI_x}^{UG}(z)$): TI_x, is measured at 70 m downstream of the Deep Green.

4. Discussion

Results from the numerical model showed that the DG wake is advected downwards as the wake propagates downstream (see Figure 9b). Due to this, there may be a reduced impact on a TST placed directly downstream compared to axis-symmetric turbines, while in the case of axis-symmetric turbines, with axial flow, the velocity deficit propagates directly downstream; hence, any power-generating device placed downstream inline will experience a reduced inflow velocity. In case of the DG wake, the advection of the low velocity wake downward and away from the trajectory center could indicate a higher inflow velocity for a downstream turbine compared to axis symmetric turbines. However, the deflection of the DG wake downward can have an impact on the bottom sedimentation/erosion in the vicinity of the DG. As seen in Figure 9c, the presence of DG increased the velocities close to the bottom compared to an undisturbed flow increasing the bottom stress. Increased bottom stress will increase bottom-generated turbulence; this, in turn, affects the wake propagation and can be addressed in the design of multi kite arrays. It should, however, be noted here that the tether attachment to the bottom large concrete block has not been considered in the LES. Further research is needed to address this more quantitatively. Moreover, since the wake does not expand much in the xy plane (see Figure 9a), the DGs could be placed closer in the y direction.

Analyzing the full ADCP observations, it could be seen that the magnitude of tidal flow speed at the trajectory center of the DG ($z = 44$ m) reaches values greater than 1.2 ms^{-1} over a significant period of the tidal cycle, indicating that the DG can be operated effectively in these periods (see Figure 10).

Whilst comparing numerical and observed data, due to the small-scale effects in tidal turbine wakes, data from the numerical model are resampled in a way similar to how the ADCP processes data using a virtual ADCP (vADCP). A few assumptions were made on the parameters used during the observations since some metadata of the observations are lacking; hence, a sensitivity study was conducted using the vADCP. vADCP parameters—mount angle, pulse length, and bin size—were varied, and their effect on the velocity and turbulence intensity was studied for undisturbed tidal flow and the DG wake flow. Higher bin sizes lead to lower resolution in both the undisturbed flow and the DG wake. Mean flow velocity and turbulence intensity in the undisturbed tidal flow was less sensitive to ADCP parameters such as beam orientation/mount angle and pulse length. In a tidal turbine wake, the orientation of the beams had a significant impact on the measured wake as it influences the regions sampled by the beams. Orientation of 0 deg measures the stream velocity in the trajectory center; and orientation 45 deg measures away from the trajectory center. Both produce very different velocity profiles. The pulse length also had a significant impact on the profiles, with higher pulse lengths producing a smoother profile. For observing tidal turbine wakes, a lower pulse length can be favored if the observation period is large enough to smoothen the uncertainties using temporal statistical analysis.

For the comparison between observational and model data, the pulse length and mount angle of the vADCP were set as 4 m and 45 deg. Under these assumptions, the velocity profiles resemble similar features. One of the discrepancies was, however, a weaker velocity deficit in the observations, which can be attributed to the lower tidal flow and higher turbulence during the observations compared to the LES set-up. The LES/ALM model underpredicted the turbulence levels in an undisturbed tidal flow, whereas the increase in turbulence due to the DG was overestimated. The turbulence intensity in both the model and the observations is increased by a factor of 2–3 from the undisturbed levels due to the presence of the DG. This can have a significant impact on DGs placed downstream if operating in the velocity deficit. High turbulence intensity can reduce the effectiveness of the control systems to maintain the DG in its trajectory and could induce fluctuations in the power generated as well. Further, it will increase the dynamical loading of the DG structures such as the wing, tether, anchor, etc., which need to be taken into account in the design phase in order to maintain the life of the components and decrease the risk of fatigue.

The ADCP beam orientations with respect to the tidal flow and the pulse length represent significant uncertainties regarding ADCP measurements. As seen in the manuscript it is also not possible to resolve the full three-dimensionality of the wake using an ADCP. A better-designed ADCP campaign (using a 5-beam ADCP) can probably aid in the more comprehensive validation of the model. ADCP combined with ADV may be one way forward. Acoustic Doppler velocimetry (ADV) can be used to obtain high-resolution, high-frequency observations. ADV measurements capture a larger range of turbulent scales compared to the ADCP. However, these instruments cannot provide the three-dimensional profile of the wake; for this, model scale experiments are useful, where the wake can be studied in a controlled environment at high temporal and spatial resolution; however, model scale experiments of the tidal turbine wakes may not scale well to full-scale real-life conditions. The wake propagation and recovery of tidal turbines in full-scale real-life conditions is still an open area of research.

As seen in this study, although the model predicts the features of the mean velocity profile and turbulence intensity in the DG wake, the wake in the ALM/LES is overestimated compared to the current ADCP data. However, since ALM/LES has been used extensively in wind turbine and farm design, this model (given the discussed uncertainties) for tidal kites could be vital in studying kite arrays and wakes.

Author Contributions: Conceptualization, N.S.S.P., S.T.F., G.B. and B.B.; methodology, N.S.S.P., S.T.F., G.B. and B.B.; formal analysis, N.S.S.P., S.T.F., G.B. and B.B.; investigation, N.S.S.P., S.T.F., G.B. and B.B.; writing—original draft preparation, N.S.S.P., S.T.F., G.B. and B.B.; writing—review and editing, N.S.S.P., S.T.F., G.B. and B.B.; visualization, N.S.S.P., S.T.F. and G.B.; supervision, S.T.F. and G.B.; project administration, S.T.F. and G.B.; funding acquisition, S.T.F., G.B. and B.B. All authors have read and agreed to the published version of the manuscript.

Funding: We acknowledge funding from Swedish Energy Agency through project P42247-2.

Data Availability Statement: The ADCP data belong to the company, Minesto AB. The OpenFOAM open-source CFD code, used for the LES simulations with Deep Green in the present work, is freely available at http://www.openfoam.org. The ALM implementation in this work is based on the libraries of turbinesFoam [36], which is a standalone user-contributed module for OpenFOAM. The adapted source code, deepGreenFoam, and the input files necessary to reproduce the present simulations are available from the authors upon request.

Acknowledgments: The computations were enabled by resources provided by the National Academic Infrastructure for Supercomputing in Sweden (NAISS) and the Swedish National Infrastructure for Computing (SNIC) at NSC, partially funded by the Swedish Research Council through grant agreements no. 2022-06725 and no. 2018-05973.

Conflicts of Interest: The authors declare no conflict of interest.

Abbreviations

Symbols	
l_{bin}	ADCP cell size [m]
l_{pulse}	ADCP pulse length [m]
$\mathbf{u} = (u, v, w)$	Velocities in the model coordinate system in x, y, and z directions [ms^{-1}]
$\mathbf{u}_a = (u_a, v_a, w_a)$	Velocities in the ADCP coordinate system [ms^{-1}]
$\mathbf{x} = (x, y, z)$	Numerical model coordinate system
$\mathbf{x}_a = (x_a, y_a, z_a)$	ADCP coordinate system
σ	Standard deviation
ξ	ADCP error velocity [ms^{-1}]
ψ	ADCP mount angle: orientation of beam with respect to the flow [deg]
Abbreviations	
ADCP	Acoustic Doppler Current Profiler
ALM	Actuator Line Model
DG	Deep Green
LES	Large Eddy Simulations

References

1. Gerkema, T. *An Introduction to Tides*; Cambridge University Press: Cambridge, MA, USA, 2019.
2. Munk, W.; Wunsch, C. Abyssal recipes II: Energetics of tidal and wind mixing. *Deep Sea Res. Part I Oceanogr. Res. Pap.* **1998**, *45*, 1977–2010. [CrossRef]
3. Coles, D.; Angeloudis, A.; Goss, Z.; Miles, J. Tidal Stream vs. Wind Energy: The Value of Cyclic Power When Combined with Short-Term Storage in Hybrid Systems. *Energies* **2021**, *14*, 1106. [CrossRef]
4. Magagna, D.; Monfardini, R. *JRC Ocean Energy Status Report 2016 Edition Technology, Market and Economic Aspects of Ocean Energy in Europe*; Publications Office of the European Union: Luxembourg, 2016.
5. Hagerman, G.; Polagye, B.; Bedard, R.; Previsic, M. Methodology for estimating tidal current energy resources and power production by tidal in-stream energy conversion (TISEC) devices. In *North American Tidal in Stream Power Feasibility Demonstration Project (TISEC) Devices (Report No. EPRI-TP-001 NA Rev 2)*; EPRI: Washington, DC, USA, 2006.
6. Encarnacion, J.I.; Johnstone, C.; Ordonez-Sanchez, S. Design of a Horizontal Axis Tidal Turbine for Less Energetic Current Velocity Profiles. *J. Mar. Sci. Eng.* **2019**, *7*, 197. [CrossRef]
7. Lewis, M.; McNaughton, J.; Márquez-Dominguez, C.; Todeschini, G.; Togneri, M.; Masters, I.; Allmark, M.; Stallard, T.; Neill, S.; Goward-Brown, A.; et al. Power variability of tidal-stream energy and implications for electricity supply. *Energy* **2019**, *183*, 1061–1074. [CrossRef]
8. Milne, I.A.; Day, A.H.; Sharma, R.N.; Flay, R.G.J. The characterisation of the hydrodynamic loads on tidal turbines due to turbulence. *Renew. Sustain. Energy Rev.* **2016**, *56*, 851–864. [CrossRef]
9. Vennell, R.; Funke, S.W.; Draper, S.; Stevens, C.; Divett, T. Designing large arrays of tidal turbines: A synthesis and review. *Renew. Sustain. Energy Rev.* **2015**, *41*, 454–472. [CrossRef]
10. Tedds, S.C.; Owen, I.; Poole, R.J. Near-wake characteristics of a model horizontal axis tidal stream turbine. *Renew. Energy* **2014**, *63*, 222–235. [CrossRef]
11. Nuernberg, M.; Tao, L. Experimental study of wake characteristics in tidal turbine arrays. *Renew. Energy* **2018**, *127*, 168–181. [CrossRef]
12. Lu, Y.; Lueck, R.G. Using a Broadband ADCP in a Tidal Channel. Part I: Mean Flow and Shear. *J. Atmos. Ocean. Technol.* **1999**, *16*, 1556–1567. [CrossRef]
13. Lu, Y.; Lueck, R.G. Using a Broadband ADCP in a Tidal Channel. Part II: Turbulence. *J. Atmos. Ocean. Technol.* **1999**, *16*, 1568–1579. [CrossRef]
14. Bourgoin, A.C.L.; Guillou, S.S.; Thiébot, J.; Ata, R. Turbulence characterization at a tidal energy site using large-eddy simulations: Case of the Alderney Race. *Philos. Trans. R. Soc. A Math. Phys. Eng. Sci.* **2020**, *378*, 20190499. [CrossRef] [PubMed]
15. Mcnaughton, J. Tidal Turbine Wake Analysis using Vessel- and Seabed-Mounted ADCPs. In Proceedings of the 5th Oxford Tidal Energy Workshop (OTE 2016), Oxford, UK, 21–22 March 2016.
16. Schmitt, P.; Elsäßer, B.; Bischof; Starzmann, R. Field testing a full-scale tidal turbine Part 2: In-line Wake Effects. In Proceedings of the European Wave and Tidal Energy Conference, Nantes, France, 6–11 September 2015.
17. Jeffcoate, P.; Starzmann, R.; Elsaesser, B.; Scholl, S.; Bischoff, S. Field measurements of a full scale tidal turbine. *Int. J. Mar. Energy* **2015**, *12*, 3–20. [CrossRef]
18. Jensen, N.O. *A Note on Wind Generator Interaction*; Risø National Laboratory: Roskilde, Denmark, 1983.
19. Katic, I.; Højstrup, J.; Jensen, N.O. A Simple Model for Cluster Efficiency. In *European Wind Energy Association Conference and Exhibition*; BT-EWEC'86. Proceedings; A. Raguzzi: Rome, Italy, 1987; Volume 1, pp. 407–410.
20. Churchfield, M.J. A review of wind turbine wake models and future directions. In Proceedings of the North American Wind Energy Academy Symposium (NAWEA'13), Boulder, CO, USA, 6–8 August 2013.
21. Jump, E.; Macleod, A.; Wills, T. Review of tidal turbine wake modelling methods: State of the art. *Int. Mar. Energy J.* **2020**, *3*, 91–100. [CrossRef]
22. Sørensen, J.N.; Shen, W.Z. Numerical Modeling of Wind Turbine Wakes. *J. Fluids Eng.* **2002**, *124*, 393–399. [CrossRef]
23. Martínez-Tossas, L.A.; Churchfield, M.J.; Leonardi, S. Large eddy simulations of the flow past wind turbines: Actuator line and disk modeling. *Wind Energy* **2015**, *18*, 1047–1060. [CrossRef]
24. Johansen, J.; Sørensen, N.N.; Michelsen, J.A.; Schreck, S. Detached-eddy simulation of flow around the NREL Phase VI blade. *Wind Energy* **2002**, *5*, 185–197. [CrossRef]
25. Vermeer, L.J.; Sørensen, J.N.; Crespo, A. Wind turbine wake aerodynamics. *Prog. Aerosp. Sci.* **2003**, *39*, 467–510. [CrossRef]
26. Barthelmie, R.J.; Hansen, K.; Frandsen, S.T.; Rathmann, O.; Schepers, J.G.; Schlez, W.; Phillips, J.; Rados, K.; Zervos, A.; Politis, E.S.; et al. Modelling and measuring flow and wind turbine wakes in large wind farms offshore. *Wind Energy* **2009**, *12*, 431–444. [CrossRef]
27. Blondel, F.; Boisard, R.; Milekovic, M.; Ferrer, G.; Lienard, C.; Teixeira, D. Validation and comparison of aerodynamic modelling approaches for wind turbines. *J. Phys. Conf. Ser.* **2016**, *753*, 022029. [CrossRef]
28. Bangga, G.; Lutz, T. Aerodynamic modeling of wind turbine loads exposed to turbulent inflow and validation with experimental data. *Energy* **2021**, *223*, 120076. [CrossRef]
29. Wu, G.; Zhang, L.; Yang, K. Development and Validation of Aerodynamic Measurement on a Horizontal Axis Wind Turbine in the Field. *Appl. Sci.* **2019**, *9*, 482. [CrossRef]

30. Salunkhe, S.; El Fajri, O.; Bhushan, S.; Thompson, D.; O'Doherty, D.; O'Doherty, T.; Mason-Jones, A. Validation of Tidal Stream Turbine Wake Predictions and Analysis of Wake Recovery Mechanism. *J. Mar. Sci. Eng.* **2019**, *7*, 362. [CrossRef]
31. Shahsavarifard, M.; Bibeau, E.L.; Chatoorgoon, V. Effect of shroud on the performance of horizontal axis hydrokinetic turbines. *Ocean Eng.* **2015**, *96*, 215–225. [CrossRef]
32. Sentchev, A.; Thiébaut, M.; Schmitt, F. Impact of turbulence on power production by a free-stream tidal turbine in real sea conditions. *Renew. Energy* **2019**, *147*, 1932–1940. [CrossRef]
33. Fredriksson, S.T.; Broström, G.; Jansson, M.; Nilsson, H.; Bergqvist, B. Large eddy simulation of the tidal power plant deep green using the actuator line method. In Proceedings of the IOP Conference Series: Materials Science and Engineering, First Conference of Computational Methods in Offshore Technology (COTech2017), Stavanger, Norway, 30 November–1 December 2017; Volume 276.
34. Fredriksson, S.T.; Broström, G.; Bergqvist, B.; Lennblad, J.; Nilsson, H. Modelling Deep Green tidal power plant using large eddy simulations and the actuator line method. *Renew. Energy* **2021**, *179*, 1140–1155. [CrossRef]
35. Draper, M.; Usera, G. Evaluation of the Actuator Line Model with coarse resolutions. *J. Phys. Conf. Ser.* **2015**, *625*, 12021. [CrossRef]
36. Gao, Z.T.; Wang, T.G. Experimental validation and improvement of actuator line model in the large-eddy simulation of wind-turbine wakes. *IOP Conf. Ser. Earth Environ. Sci.* **2020**, *463*, 012113. [CrossRef]
37. Mendoza, V.; Goude, A. Validation of Actuator Line and Vortex Models using Normal Forces Measurements of a Straight-Bladed Vertical Axis Wind Turbine. *Energies* **2020**, *13*, 511. [CrossRef]
38. OpenFOAM. The OpenFOAM Foundation. Available online: https://openfoam.org/ (accessed on 14 August 2023).
39. Bachant, P.; Goude, A.; daa-mec; Wosnik, M. turbinesFoam/turbinesFoam: v0.1.1. November 2019. Available online: https://zenodo.org/record/3542301#.ZCbaUspBxaQ (accessed on 14 August 2023).
40. De Villiers, E. *The Potential of Large Eddy Simulation for the Modeling of Wall Bounded Flows Eugene de Villiers*; Imperial College London: London, UK, 2006.
41. Moeng, C.H.; Sullivan, P.P. NUMERICAL MODELS | Large-Eddy Simulation. In *Encyclopedia of Atmospheric Sciences*, 2nd ed.; Elsevier: Boulder, CO, USA, 2015; pp. 232–240.
42. Bachant, P.; Goude, A.; Wosnik, M. Actuator line modeling of vertical-axis turbines. *arXiv* **2016**, arXiv:1605.01449.
43. Blocken, B.; Stathopoulos, T.; Carmeliet, J. CFD simulation of the atmospheric boundary layer: Wall function problems. *Atmos. Environ.* **2007**, *41*, 238–252. [CrossRef]
44. Muste, M.; Yu, K.; Spasojevic, M. Practical aspects of ADCP data use for quantification of mean river flow characteristics; Part I: Moving-vessel measurements. *Flow Meas. Instrum.* **2004**, *15*, 1–16. [CrossRef]
45. Mueller, D.S. Field Assessment of Acoustic-Doppler Based Discharge Measurements. In Proceedings of the Hydraulic Measurements and Experimental Methods Specialty Conference (HMEM) 2002, Estes Park, CO, USA, 28 July–1 August 2002; pp. 23–31.
46. Yorke, T.H.; Oberg, K.A. Measuring river velocity and discharge with acoustic Doppler profilers. *Flow Meas. Instrum.* **2002**, *13*, 191–195. [CrossRef]
47. Oberg, K.; Mueller, D.S. Validation of Streamflow Measurements Made with Acoustic Doppler Current Profilers. *J. Hydraul. Eng.* **2007**, *133*, 1421–1432. [CrossRef]
48. *P/N 951-6069-00*; Acoustic Doppler Current Profiler Principles of Operation—A Practical Primer. Teledyne RD Instruments, Inc.: Poway, CA, USA, 2011.
49. Stacey, M.T.; Monismith, S.G.; Burau, J.R. Measurements of Reynolds stress profiles in unstratified tidal flow. *J. Geophys. Res. Ocean* **1999**, *104*, 10933–10949. [CrossRef]
50. Mercier, P.; Thiébaut, M.; Guillou, S.; Maisondieu, C.; Poizot, E.; Pieterse, A.; Thiébot, J.; Filipot, J.-F.; Grondeau, M. Turbulence measurements: An assessment of Acoustic Doppler Current Profiler accuracy in rough environment. *Ocean Eng.* **2021**, *226*, 108819. [CrossRef]
51. Mueller, D.; Abad, J.; García, C.; Gartner, J.; García, M.; Oberg, K. Errors in Acoustic Doppler Profiler Velocity Measurements Caused by Flow Disturbance. *J. Hydraul. Eng.* **2007**, *133*, 1411–1420. [CrossRef]
52. Thiébaut, M.; Filipot, J.F.; Maisondieu, C.; Damblans, G.; Jochum, C.; Kilcher, L.F.; Guillou, S. Characterization of the vertical evolution of the three-dimensional turbulence for fatigue design of tidal turbines. *Philos. Trans. R. Soc. A Math. Phys. Eng. Sci.* **2020**, *378*, 20190495. [CrossRef]
53. Thiébaut, M.; Filipot, J.F.; Maisondieu, C.; Damblans, G.; Duarte, R.; Droniou, E.; Guillou, S. Assessing the turbulent kinetic energy budget in an energetic tidal flow from measurements of coupled ADCPs. *Philos. Trans. R. Soc. A Math. Phys. Eng. Sci.* **2020**, *378*, 20190496. [CrossRef]
54. Durgesh, V.; Thomson, J.; Richmond, M.C.; Polagye, B.L. Noise correction of turbulent spectra obtained from acoustic doppler velocimeters. *Flow Meas. Instrum.* **2014**, *37*, 29–41. [CrossRef]
55. Nystrom, E.A.; Rehmann, C.R.; Oberg, K.A. Evaluation of Mean Velocity and Turbulence Measurements with ADCPs. *J. Hydraul. Eng.* **2007**, *133*, 1310–1318. [CrossRef]
56. Crismer, J.-B.; Trigaux, F.; Duponcheel, M.; Winckelmans, G. Large-Eddy Simulation of airborne wind energy systems wakes. *J. Phys. Conf. Ser.* **2023**, *2505*, 12036. [CrossRef]
57. Fredriksson, S.T.; Brostrom, G.; Bergqvist, B.; Lennblad, J.; Nilsson, H. Turbulence Characteristics in Tidal Flows Using LES and ALM to Model the Tidal Power Plant Deep Green. In Proceedings of the 4th Asian Wave & Tidal Energy Conference (AWTEC 2018), Taipei, Taiwan, 9–13 September 2018.

58. Frandsen, S.; Barthelmie, R.; Pryor, S.; Rathmann, O.; Larsen, S.; Højstrup, J.; Thøgersen, M. Analytical modelling of wind speed deficit in large offshore wind farms. *Wind Energy* **2006**, *9*, 39–53. [CrossRef]
59. Ouro, P.; Stoesser, T. Impact of Environmental Turbulence on the Performance and Loadings of a Tidal Stream Turbine. *Flow Turbul. Combust.* **2019**, *102*, 613–639. [CrossRef]